Polycyclic aromatic hydrocarbons in Seyfert and star-forming galaxies

I. García-Bernete [ORCID],[1]★ D. Rigopoulou,[1] A. Alonso-Herrero,[2] M. Pereira-Santaella [ORCID],[3] P. F. Roche[1]
and B. Kerkeni[1,4,5]

[1]*Department of Physics, University of Oxford, Oxford OX1 3RH, UK*
[2]*Centro de Astrobiología, CSIC-INTA, ESAC Campus, E-28692, Villanueva de la Cañada, Madrid, Spain*
[3]*Centro de Astrobiología, CSIC-INTA, Carretera de Torrejón a Ajalvir, E-28880 Torrejón de Ardoz, Madrid, Spain*
[4]*Département de Physique, LPMC, Faculté des Sciences de Tunis, Université de Tunis el Manar, Tunis 2092, Tunisia*
[5]*ISAMM, Université de la Manouba, La Manouba 2010 Tunisia*

ABSTRACT

Polycyclic Aromatic Hydrocarbons (PAHs) are carbon-based molecules resulting from the union of aromatic rings and related species, which are likely responsible for strong infrared emission features. In this work, using a sample of 50 Seyfert galaxies ($D_L < 100$ Mpc) we compare the circumnuclear (inner kpc) PAH emission of AGN to that of a control sample of star-forming galaxies (22 luminous infrared galaxies and 30 H II galaxies), and investigate the differences between central and extended PAH emission. Using Spitzer/InfraRed Spectrograph spectral data of Seyfert and star-forming galaxies and newly developed PAH diagnostic model grids, derived from theoretical spectra, we compare the predicted and observed PAH ratios. We find that star-forming galaxies and AGN-dominated systems are located in different regions of the PAH diagnostic diagrams. This suggests that not only are the size and charge of the PAH molecules different, but also the nature and hardness of the radiation field that excite them. We find tentative evidence that PAH ratios in AGN-dominated systems are consistent with emission from larger PAH molecules ($N_c > 300$–400) as well as neutral species. By subtracting the spectrum of the central source from the total, we compare the PAH emission in the central versus extended region of a small sample of AGN. In contrast to the findings for the central regions of AGN-dominated systems, the PAH ratios measured in the extended regions of both type 1 and type 2 Seyfert galaxies can be explained assuming similar PAH molecular size distribution and ionized fractions of molecules to those seen in central regions of star-forming galaxies ($100 < N_c < 300$).

Key words: Galaxies: active – Galaxies: nuclei – Galaxies: Seyfert – Galaxies: star formation – Infrared: galaxies.

1 INTRODUCTION

Previous infrared (IR) observations have demonstrated that Polycyclic Aromatic Hydrocarbons (PAH) features are ubiquitous in a variety of astrophysical objects and environments. Indeed, the variation between PAH features indicate different physical conditions (see e.g. Li 2020 for a review). Recently, Rigopoulou et al. (2021) presented newly developed PAH diagnostic grids derived from theoretically computed PAH spectra (see also Maragkoudakis, Peeters & Ricca 2020). These grids enable disentangling the properties of the PAH molecules such as the size of the molecule, its ionization fraction and, the hardness of the radiation field.

PAH molecules absorb a significant fraction of ultraviolet (UV)/optical photons resulting in their excitation. The excited molecules produce IR features via vibrational relaxation (e.g. Draine & Li 2007). PAH molecules are likely responsible for the family of strong IR emission features (3.3, 6.2, 7.7, 8.6, 11.3, and 12.7 μm; e.g. Tielens 2008) observed in Galactic and extragalactic sources. PAHs are abundant ($\sim 10^{-7}$ relative to H; e.g. Allamandola, Tielens & Barker 1989) and they account for up to 20 per cent of the total IR emission of metal rich galaxies (Smith et al. 2007a). Interestingly, these molecules are considered the building blocks of the larger interstellar dust grains (e.g. Tielens 2013).

The 3.3, 8.6, and 11.3 μm bands are attributed to the stretching modes of C–H bonds, whereas 6.2 and 7.7 μm bands are due to C–C bond (e.g. Allamandola et al. 1989). Previous studies used the 6.2 and 7.7 μm features as a diagnostic of PAH molecular size (e.g. Jourdain de Muizon, D'Hendecourt & Geballe 1990; Draine & Li 2001; Sales, Pastoriza & Riffel 2010; Draine et al. 2020; Rigopoulou et al. 2021). Recently, the 11.3/3.3 PAH ratio has also been proposed as a PAH molecule size indicator (Maragkoudakis et al. 2020). Moreover, Rigopoulou et al. (2021) found that the dependency of the 11.3/3.3 PAH ratio with the molecular size is not a linear one, and that the tight relation with the number of carbons for small molecules ($N_c < 100$) progressively flattens for larger molecules. These authors also found a tight correlation with the intensity of the radiation field with the 11.3/3.3 PAH ratio decreasing with increasing energy.

It is well established that ionization dramatically enhances the emission in the 6–9 μm region, suggesting that these IR bands result from highly vibrationally excited cations, while the 3.3, 8.6, and 11.3 μm features originate mostly from neutral PAH molecules (e.g. Allamandola et al. 1989; Draine & Li 2001; Draine et al. 2020). Therefore, the ratios between the 11.3 μm feature and those related to

★ E-mail: igbernete@gmail.com

the charged PAHs (i.e. 6.2 or 7.7 μm features) have been proposed as a good indicator of the PAH ionization fraction (e.g. Draine & Li 2001; Galliano et al. 2008; Draine et al. 2020; Rigopoulou et al. 2021).

PAH features are often used to measure the star formation rate (SFR) of galaxies (see e.g. Rigopoulou et al. 1999; Peeters, Spoon & Tielens 2004; Wu et al. 2005) but also in AGN (see e.g. Diamond-Stanic & Rieke 2012; Esquej et al. 2014). In addition, low ionization potential (IP) mid-infrared (MIR) emission lines such as [Ne II] λ12.81 μm have been used as an SFR indicator in AGN (e.g. Spinoglio, Andreani & Malkan 2002; Ho & Keto 2007; Pereira-Santaella et al. 2010a). However, this emission line could be significantly contaminated by the AGN (García-Bernete et al. 2017). These SFR indicators are mainly important in the vicinity of AGN-dominated systems where classical SF indicators normally fail. In a study by Jensen et al. (2017) the authors suggest that PAH molecules can also be excited by AGN photons. If this is indeed the case, then the use of PAH emission as an SFR tracer needs to be re-evaluated.

In this work, we employ the newly computed PAH grids presented in Rigopoulou et al. (2021) to investigate the properties of the PAH emitting molecules in a sample of AGN (our main sample) and a *control sample* of star-forming galaxies with no AGN detections. Our AGN sample includes Seyfert galaxies with a wide range of properties (see Section 2) enabling us to obtain statistically significant results. The control sample of star-forming galaxies has a similar redshift distribution. Our aim is to study the effect of the nuclear activity on the properties of the PAH molecules located in the central/extended regions of AGN and also in star-forming galaxies.

The paper is organized as follows. Sections 2 and 3 describe the sample selection and the observations used in this study, respectively. The MIR spectral modelling and spectral decomposition are presented in Sections 4 and 5. The main results of the PAH emission are presented in Section 6. In Section 7, we compare the PAH band ratios of AGN and star-forming galaxies with the theoretical models. In Section 8, we compare the average PAH spectra of the different source groups. Finally, in Section 9, we summarize the main conclusions of this work. Throughout this paper, we assumed a cosmology with H_0=70 km s^{-1} Mpc^{-1}, Ω_m=0.3, and Ω_Λ=0.7, and a velocity-field corrected using the Mould et al. (2000) model, which includes the influence of the Virgo cluster, the Great Attractor, and the Shapley supercluster.

2 SAMPLE SELECTION

2.1 Seyfert sample

The main aim of this work is to study the properties of the PAH molecules located in the central/extended regions of AGN and compare them with those in star-forming galaxies. Therefore, we first focus on building a representative sample of Sy galaxies sampling the different Seyfert properties. For the Sy galaxy sample we used the ultra-hard 14–195 keV band of the nine-month catalog, which is observed with Swift/BAT (Tueller et al. 2008). The catalog is far less sensitive to the effects of obscuration than optical or softer X-ray wavelengths, making this AGN selection one of the least biased for $N_H < 10^{24}$ cm^{-2} to date (see e.g. Winter et al. 2009, 2010; Weaver et al. 2010; Ichikawa et al. 2012; Ricci et al. 2015; Ueda et al. 2015). We note that this catalog covers 80 per cent of the sky with a flux threshold of 3.5×10^{-11} erg cm^{-2} s^{-1} in the 14–195 keV band and covers one-third of the sky near the ecliptic poles at 2.5×10^{-11} erg cm^{-2} s^{-1}. The Swift/BAT sources were selected based on detection at 4.8σ or higher. Therefore, the catalog is flux-limited in the 14–195 keV X-ray band and consists of 153 sources.

We note that we have excluded from this work broad-absorption line (BAL) quasars because their inner region geometry is thought to be significantly different from standard AGN.

Since in this work we are interested in the study of the effect of the AGN in the central and extended emission of Seyfert galaxies, we mainly focused on type-1 Seyfert galaxies (i.e. Sy1, Sy1.2, and Sy1.5; hereafter Sy1). To this end, we first selected all the Sy1 from the parent Swift/BAT sample (69 sources). From these we culled sources with luminosity distances $D_L < 100$ Mpc (29 sources). Finally, we cross-correlated these sources with the Spitzer Heritage Archive (SHA)[1] to select those with available Spitzer/Infrared Spectrograph (IRS) MIR spectra covering the 5–35 μm range (i.e. observed in the short- and long-low modules) with the IRS instrument (Houck et al. 2004). The final Swift/BAT Sy1 sample comprises 23 objects (excluding NGC 7213 which exhibits very strong silicate emission).

However, the above mentioned flux threshold of the Swift/BAT catalog excludes relatively low-luminosity Seyfert galaxies, which are present in the local Universe. Therefore, to counteract this effect, we augmented our original sample with Seyfert galaxies from the RSA sample (Maiolino & Rieke 1995). This results in five more type-1 Seyfert galaxies with $D_L < 100$ Mpc (namely, ESO 323-G77, NGC 1097, NGC 1566, NGC 4235, & UGC 3478). Therefore, our final sample contains 28 Sy1 galaxies.

Although our focus is on Sy1 galaxies we are also interested in sampling a wide range of Seyfert properties. Thus, we added 11 Sy1.8/1.9 and 11 Sy2 galaxies from the RSA sample (13 objects) and the Swift/BAT catalog (9 objects). These additional Seyferts have similar luminosities, inclinations and satisfy the same distance limit as the original Sy1 sample.

Taking into account the spatial scale probed by Spitzer/IRS ($\sim$4–6 arcsec) and the distance limit selected, this allows us to study the inner central kpc of these galaxies. The final sample used in this paper comprises 50 local Seyfert galaxies. The majority of the observations (36/50) employed in this work were observed in the low-resolution (R$\sim$60–120) IRS spectral mapping mode, and the rest of the data were observed in the staring mode (see Section 3).

In Fig. 1, we present the range of X-ray hydrogen column densities, bolometric luminosities and strengths of the 9.7 μm silicate feature for our sample. Note that column densities of $N_H^{X-ray} = 10^{20}$ cm^{-2} correspond to the lowest values reported by Ricci et al. (2017). This shows that our selected AGN sample probes well the observed ranges for the various types of Seyfert galaxies. The sample sorted by right ascension (R.A.) is shown in Table 1.

In summary, our sample covers an AGN luminosity range of $\log(L_{bol}^{14-195\ keV}) \sim$41.0–45.5 erg s^{-1} and luminosity distances $D_L < 100$ Mpc. We note that there are no statistically significant differences between the distances for the various Sy groups according to the Kolmogorov-Smirnov (KS) test. As expected, we find that the 92 per cent of Sy1 galaxies in our sample have lower values of X-ray hydrogen column densities ($N_H^{X-ray} < 10^{22}$ cm^{-2}), in comparison with the 60 per cent and 20 per cent for Sy1.8/1.9 and Sy2 galaxies, respectively. We find that this difference is statistically significant using the Fisher's exact test.

2.2 Star-forming control sample

For the present study, we also selected a control sample of star-forming galaxies that span similar redshifts and total IR luminosities as the Seyfert sample (see Fig. 2). We selected luminous infrared
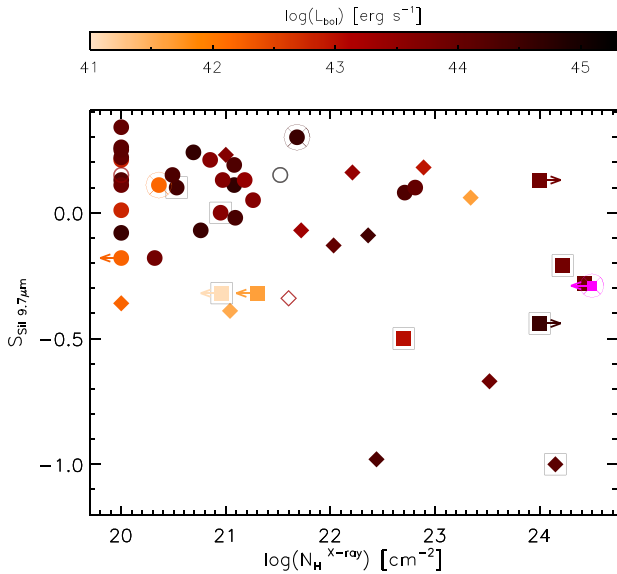
---

[1] https://sha.ipac.caltech.edu/applications/Spitzer/SHA/

Figure 1. The strength of the 9.7 μm silicate feature (see Section 6) versus the X-ray hydrogen column density (see Table 1 for references). The silicate strength is computed as $S_{Sil} = \ln(f_{9.7}/f_{cont})$. Colour-coded symbols represent the bolometric luminosity. The magenta data point correspond to the only galaxy with no X-ray flux detected (i.e. NGC 5953). Filled circles, diamond, and squares correspond with Sy1, Sy1.8/1.9, and Sy2, respectively. Note that open black squares and circles with X represent galaxies that have been also classified as AGN/SF composite and LINER, respectively. Finally, open circles and diamond correspond with Sy1 and Sy1.8/1.9 without any PAH bands detected within the 11.3 μm PAH complex (11.23 and 11.33 μm features) in the Spitzer/IRS spectra, respectively. Note that all Sy2 galaxies show the 11.3 μm PAH feature in the Spitzer/IRS spectra.

galaxies (LIRGs) and H II galaxies from the Great Observatories All-sky LIRG Survey (GOALS; Armus et al. 2009), Brandl et al. (2006) and the Spitzer Infrared Nearby Galaxies Survey (SINGS; Kennicutt et al. 2003).

The GOALS sample consist of a complete subset of the Infrared Astronomical Satellite (IRAS) Revised Bright Galaxy Sample (RBGS; Sanders et al. 2003). The LIRGs within GOALS cover different interaction stages and nuclear spectral types. For our study, we selected 21 LIRGs from the GOALS sample that have Spitzer/IRS observations and are not interacting or classified as AGN and/or LINER. To select H II galaxies, we used the SINGS sub-sample (23 sources) presented in Smith et al. (2007a), which was observed with Spitzer/IRS.

We also use an additional sample of 22 star-forming galaxies observed with Spitzer/IRS (Brandl et al. 2006). By removing those sources classified as AGN/SF composite in Brandl et al. (2006), we add one LIRG and 7 H II galaxies (sub-LIRGs; log (L_{IR}) < 11 L$_{\odot}$) to the control sample. Therefore, the final star-forming control sample consists of 22 LIRGs and 30 H II galaxies. In the following, we consider the star-forming control sample as the combination of these two samples (i.e. 52 galaxies).

3 OBSERVATIONS

In what follows we describe the IR observations used in this work.

3.1 Archival data

3.1.1 *Spitzer Space Telescope MIR spectra*

The majority of the Seyfert galaxies (36/50) in our AGN sample and 2 LIRGs from our control sample of star-forming galaxies with extended MIR emission (see Section 2.2) were observed in the spectral mapping mode. We used the low (R~60–120) resolution IRS modules: short-low (SL1; 7.4–14.5 μm, SL2; 5.2–7.7 μm) and long-low (LL1; 19.5–38.0 μm, LL2; 14.0–21.3 μm). We downloaded the Basic Calibrated Data (BCD) from the SHA archive, which are processed by the Spitzer pipeline.

In the case of galaxies with spectral mapping observations available, we used CUBISM (Smith et al. 2007b) to perform sky background subtraction, rejection of rogue pixels, flux calibration and estimates of the statistical uncertainty at each wavelength and, finally, to combine the various slit observations and build the spectral cubes.

Using these spectral cubes and assuming that the AGN emission is unresolved, we extracted 1-D central spectra treating the AGN as a point-like source. For the extraction we used square apertures of 5.9 arcsec × 5.9 arcsec and 17.3 arcsec × 17.3 arcsec for the SL and LL modules, respectively. Then we applied an aperture correction to account for slit losses using a standard star, which is equivalent to a point source extraction and provides the best signal-to-noise ratio (S/N). For those galaxies showing extended emission in the spectral mapping data, we extracted a second spectrum using an aperture containing the total flux (see Fig. 3). Then, for these galaxies, we derived the extended emission spectrum by subtracting the central spectrum (point-like extraction) from the total one to remove the contribution of the point-like source.

Note that 2 LIRGs (NGC 3110 and NGC 6701) within our star-forming control sample have available Spitzer spectral mapping observations and they show extended MIR emission (Pereira-Santaella et al. 2010b). Thus, we also derived their extended emission and central spectra using the method described above.

For the star-forming galaxies selected from Brandl et al. (2006) and the remainder of the AGN sample, we retrieved low-resolution MIR staring spectra from the Cornell Atlas of Spitzer/IRS Source (CASSIS, version LR7; Lebouteiller et al. 2011). The spectra were reduced with the CASSIS software, using the optimal extraction to get the best S/N, which is equivalent to a point source extraction. Finally for comparison, we also retrieved low-resolution MIR staring spectra from CASSIS of six planetary nebulae (PNe) selected from Stanghellini et al. (2007), these are discussed in Section 8.

Note that for both spectral mapping and staring point-like extractions we only needed to apply a small offset to stitch together the different modules (SL/LL; ≲10 per cent).

3.1.2 *Spitzer Space Telescope MIR imaging*

We compiled MIR images of the AGN sample obtained with the Infrared Array Camera (IRAC; Fazio et al. 2004) using the 3.6 and 8 μm channels (angular resolution ~1.9 arcsec). The IRAC FOV is 5.2 arcmin × 5.5 arcmin on the sky and its pixel scale is 1.2 arcsec. We downloaded the reduced and calibrated mosaiced data from the SHA archive. Note that these mosaics are re-sampled to a pixel size of 0.6 arcsec.

3.2 Literature data

The 12, 25, 60, and 100 μm IRAS fluxes were taken from the IRAS RBGS (Sanders et al. 2003) and the IRAS Point Source

Table 1. Seyfert sample. R.A., declination (Dec.). The luminosity distance and spatial scale were calculated using a cosmology with $H_0 = 70$ km s^{-1} Mpc^{-1}, $\Omega_m = 0.3$, and $\Omega_\Lambda = 0.7$, and a velocity-field corrected using the Mould et al. (2000) model, which includes the influence of the Virgo cluster, the Great Attractor, and the Shapley supercluster. † This galaxy is part of the Virgo cluster (Binggeli, Sandage & Tammann 1985). Galaxy inclination were taken from Whittle (1992) when available, otherwise from HyperLeda data base. N_H^{X-rays} corresponds to the foreground extinction due to the host galaxy. The N_H^{X-ray} were taken from Ricci et al. (2017) when possible otherwise are indicated by superscripts. N_H^{X-ray} references: a) Nemmen et al. (2006); b) Brightman & Nandra (2011); c) Cappi et al. (2006); d) Guainazzi, Matt & Perola (2005); e) Risaliti, Maiolino & Salvati (1999); f) Shu et al. (2007); g) Bassani et al. (1999). Spectral type were taken from Véron-Cetty & Véron (2006) when possible, otherwise from Tueller et al. (2008) which are indicated by ∗ symbol. The only exceptions are NGC 3786, NGC 3982, NGC 4639, Fairall 49, and UGC 3478 classifications which were taken from Maiolino & Rieke (1995). Note that LINERb classification means LINER with broad Balmer lines, and the i, h, and n subscripts correspond to Sy1 with detected broad Paschen lines (in the IR spectra), narrow-lines, and broad polarized Balmer lines, respectively. AGN/SF composites, based on their UV emission and/or emission line ratios, are denoted by "comp". References: h) Sosa-Brito et al. (2001); i) Gonzalez Delgado & Perez (1997); j) Rodríguez-Ardila & Viegas (2003); k) González Delgado, Heckman & Leitherer (2001); l) Yuan, Kewley & Sanders (2010); m) Wilson et al. (1991); n) Díaz-Santos et al. (2007).

| Name	R.A. (J2000)	Dec. (J2000)	D_L (Mpc)	Spatial scale (pc arcsec^{-1})	Inclination (deg)	log N_H^{X-ray} (cm^{-2})	Spectral type
(1)	(2)	(3)	(4)	(5)	(6)	(7)	(8)
Mrk 352	00h59min53.3s	31d49h37s	62.5	303	34	20.0	1.0∗
NGC 931	02h28min14.5s	31d18min42s	69.5	337	81	21.09	1.5∗
NGC 1097	02h46min19.0s	−30d16min28s	17.2	83	55	20.36[a]	LINERb/1.0∗
NGC 1275	03h19min48.2s	+41d30min42s	73.9	358	58	21.68	1.5 /2.0∗/LINER[h]
NGC 1365	03h33min36.4s	−36d08min24s	22.4	108	46	22.21	1.8
ESO 548-G081	03h42min03.7s	−21d14min40s	60.7	294	64	20.0	1.0∗
NGC 1566	04h20min00.7s	−54d56min17s	20.2	98	38	20.0	1.5
NGC 1667	04h48min37.2s	−06d19min12s	63.8	310	38	24.43[b]	2.0
MCG-01-13-025	04h51min41.5s	−03d48min34s	66.9	324	50	20.0	1.2∗
4U0517+17	05h10min45.5s	+16d29min55.7s	75.5	366	45	21.08	1.5∗
ESO 362-G018	05h19min35.8s	−32d39min28s	53.4	259	71	20.0	1.5∗
UGC 3478	06h32min47.2s	+63d40min25S	57.0	276	77	21.18	1.2
Mrk 6	06h52min12.2s	74d25min38s	82.9	402	63	20.76	1.5∗
Mrk 79	07h42min32.8s	49d48min35s	97.1	471	37	20.0	1.2∗
NGC 2992	09h45min42.0s	−14d19min35s	35.6	173	62	21.72	1i/2.0∗
NGC 3227	10h23min30.6s	+19d51min56s	21.2	103	57	20.95	1.5/comp[i,j]
NGC 3516	11h06min47.4s	+72d34min07s	43.1	209	44	20.0	1.5
NGC 3783	11h39min01.8s	−37d44min19s	37.7	183	37	20.49	1.5/1.0∗
NGC 3786	11h39min42.5s	+31d54min33s	45.5	221	65	22.36	1.8
UGC 6728	11h45min16.0s	+79d40min53s	33.2	161	56	20.00	1.2∗
NGC 3982	11h56min28.1s	+55d07min30s	22.7	110	29	23.34[b]	2.0
NGC 4051	12h03min09.6s	+44d31min53s	13.5	65	40	20.0	1n/1.5∗
NGC 4138	12h09min29.9s	+43d41min06s	18.4	89	61	22.89	1.9
NGC 4151	12h10min32.5s	+39d24min21s	20.8	101	26	22.71	1.5
NGC 4235	12h17min09.9s	+07d11min29s	40.8	198	90	21.26	1.2
NGC 4253 (Mrk 766)	12h18min26.5s	29d48min46s	63.2	306	44	20.32	1.5∗
NGC 4388†	12h25min46.7s	+12d39min41s	17.0	82	78	23.52	1h/2.0∗
NGC 4395	12h25min48.9s	+33d32min48s	4.0	19	90	21.04	1.8/1.9∗
NGC 4501	12h31min59.3s	+14d25min13s	14.6	71	63	<21.3[c]	2.0
NGC 4593	12h39min39.4s	−05d20min39s	43.1	209	40	20.0	1.0
NGC 4639	12h42min52.5s	+13d15min25s	14.5	70	51	<20.00[c]	1.8
ESO 323-G77	13h06min26.2s	−40d24min52s	62.1	301	60	22.81	1.2
NGC 5033	13h13min27.5s	+36d35min38s	18.0	87	65	20.00	1.8
NGC 5135	13h25min44.0s	−29d50min02s	60.2	292	24	>24.00[d]	2.0/comp[k]
MCG-06-30-015	13h35min53.8s	−34d17min44s	27.8	135	59	20.85	1.2∗
IC 4329A	13h49min19.3s	−30d18min34s	82.0	397	66	21.52	1.2
NGC 5347	13h53min17.8s	+33d29min27s	41.7	202	45	>24.00[e]	2.0
NGC 5506	14h13min14.8s	−03d12min26s	31.2	151	90	22.44	1i/1.9∗
NGC 5548	14h17min59.6s	+25d08min13s	82.5	400	33	20.69	1.5
NGC 5953	15h34min32.3s	+15d11min38s	35.7	173	44	...	2.0/LINER[l]
IRAS 18325-5926 (Fairall49)	18h36min58.3s	59d24min09s	92.1	50	22.03	446	1.8
NGC 6814	19h42min40.7s	−10d19min23s	26.7	130	20	20.97	1.5
NGC 6860	20h08min47.1s	−61d06min00s	68.0	330	58	21.08	1.5/1.0∗
NGC 6890	20h18min18.1s	−44d48min24s	37.2	180	38	21.00[b]	1.9
NGC 7130	21h48min19.5s	−34d57min05s	72.6	340	34	24.22	2.0/comp[k]
NGC 7314	22h35min46.1s	−26d03min02s	21.7	105	65	21.6	1h/1.9∗
NGC 7469	23h03min15.6s	+08d52min26s	69.9	339	53	20.53	1.5/1.2∗/comp[n,m]
NGC 7496	23h09min47.3s	−43d25min40s	24.1	117	53	22.70[f]	2.0/comp[l]
NGC 7582	23h18min23.5s	−42d22min14s	22.9	111	62	24.15	1i/2.0∗/comp[l]
NGC 7590	23h18min54.8s	−42d14min21s	22.9	111	69	<20.96[g]	2.0/comp[l]
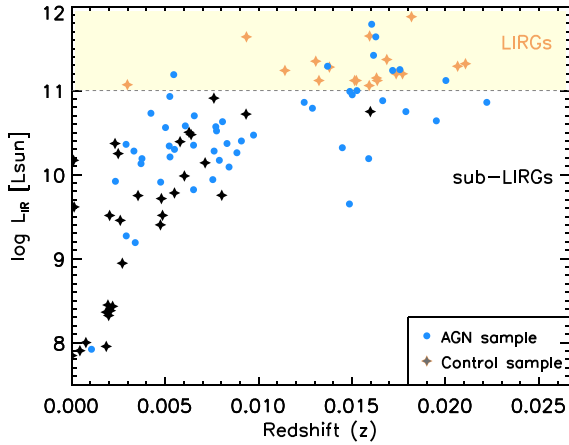
Figure 2. Total IR luminosity versus redshift for all the sources used in this work. Filled stars and blue circles correspond to the star-forming control sample and AGN sample. Black stars and orange stars indicate H II galaxies (sub-LIRGs) and LIRGs. The shaded yellow region corresponds to the LIRG luminosity region.
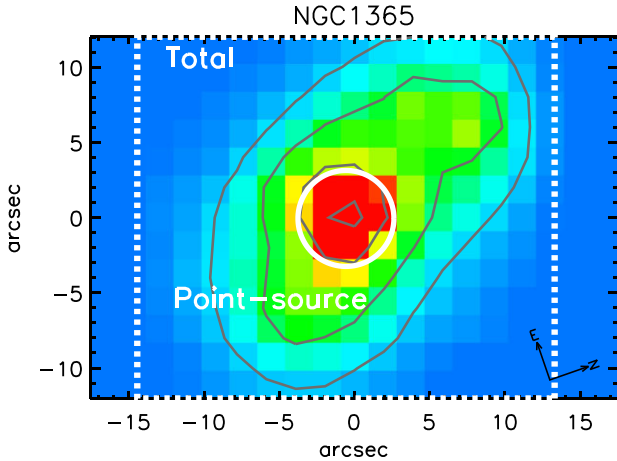

Figure 3. Schema of the different apertures used to calculate the central and extended emission of our sample. The apertures are overplotted on the 10 μm Spitzer/IRS map (using 1 μm window) of NGC 1365. The white dashed region and solid circle correspond to the apertures used to calculate the fluxes of the total galaxy emission and the central point-like component that is subtracted from the former to remove the AGN contribution, respectively. The extended emission spectrum is calculated by subtracting the central emission from the total emission.

Catalog[2] (IRAS PSC; Helou et al. 1986). Note that IRAS data were obtained with 0.6-m telescope, with a pixel size of 2 arcmin and an angular resolution ranging from 4 to 6 arcmin. We also collected IR ~3.4, 4.6, and 12 μm photometry from the All-Sky Data Release Point Source Catalog[3]. These data were taken with the 0.4-m Wide-field Infrared Survey Explorer telescope (WISE; Wright et al. 2010), which has an FoV of 47 arcmin × 47 arcmin on the sky and its pixel scale is 2.75 arcsec.

We retrieve 6.2, 7.7, and 11.3 μm PAH fluxes for the LIRGs from GOALS and for the H II galaxies from SINGS. Note that these values were calculated using the same methodology as in our work

(see Section 4). We refer the reader to Smith et al. (2007a) and Armus et al. (2009) for details of the observations. The PAH λ3.3 μm fluxes for the samples of H II galaxies and LIRGs were taken from Ichikawa et al. (2014) and Inami et al. (2018), respectively, and, were observed using AKARI and an aperture to match the Spitzer/IRS slit.

Finally, we compiled PAH λ3.3 μm feature measurements available in the literature for our AGN sample (see Table A1 in Appendix A). The 3.3 μm PAH band fluxes are both from ground- and space-based data (see Table A1). Ground-based spectra were obtained with the SpeX spectrograph (Rayner et al. 2003) on the 3.0–m NASA IR Telescope Facility (IRTF) and space-based spectra with the IR camera (IRC) on-board the Japanese IR astronomy satellite AKARI (Murakami et al. 2007; Onaka et al. 2007) and the Short Wavelength Spectrometer (SWS) on board the IR Space Observatory (*ISO*; Kessler et al. 1996). Smith et al. (2007a) found that the fractional power of the PAH features to the IRAC 8 μm band is ∼70 per cent in SINGS galaxies. Therefore, we made the reasonable assumption that the emission of the various PAH features are co-spatial and can be traced by the IRAC 8 μm band. Following the methodology presented in McKinney et al. (2021) we projected the Spitzer/IRS aperture and those used for deriving the PAH λ3.3 μm feature emission on to the IRAC 8 μm images. To estimate the aperture matching correction we used the ratio between the two apertures. A large fraction of the sample have IRAC 8 μm data, but we used the IRAC 3.6 μm band when there is no 8 μm images available or the central part of the image is saturated (i.e. NGC 1365, NGC 4593, MCG-06-30-015, and NGC 7469).[4] Note that for NGC 5506 and NGC 7582 both IRAC 3.6 and 8 μm images are saturated, and thus we used the median aperture matching correction.

4 MIR MODELLING

PAHFIT (Smith et al. 2007a) is a selection of routines to fit the MIR continuum and the dust emission features of the Spitzer/IRS MIR spectra. In brief, PAHFIT includes thermal continuum radiation from dust grains, fine-structure lines, H_2 lines, PAH features, and the extinction profile which includes silicate in absorption. However, the original version of PAHFIT did not include silicates in emission, which is a key feature in type 1 AGN. Therefore, in this work, we use a modified version of the PAHFIT code that also includes the 10 and 18 μm silicate features in emission (see e.g. Baum et al. 2010; Diamond-Stanic & Rieke 2010; Gallimore et al. 2010; LaMassa et al. 2010; Dicken et al. 2012, 2014; Sales et al. 2014; Lyu & Rieke 2018; Alonso-Herrero et al. 2020; Gleisinger et al. 2020). We follow the same methodology as presented in Gleisinger et al. (2020) to obtain the fluxes of the different PAH bands and emission lines from the Spitzer/IRS MIR spectra of our sample of AGN and star-forming galaxies from Brandl et al. (2006).

This version of PAHFIT uses a Markov chain Monte Carlo technique to evaluate the parameter uncertainties. It also makes use of the DREAM(Z) stepping algorithm (ter Braak et al. 2008), which performs self-adaptive steps through parameter space. The code employs the Metropolis likelihood criterion (Metropolis et al. 1953) to decide whether or not to keep the next set of parameters in the chain. This version of PAHFIT has been already tested in Gleisinger et al. (2020) for a sample of AGN using Spitzer/IRS MIR spectra (see their fig. 1). We note that the Spitzer/IRS spectra of the majority of the galaxies in this sample have been previously studied (e.g. Baum et al. 2010; Diamond-Stanic & Rieke 2010; Gallimore et al. 2010;

[4]Note that for those galaxies with both channel images available we find practically the same ratios using IRAC 3.6 and 8 μm data.
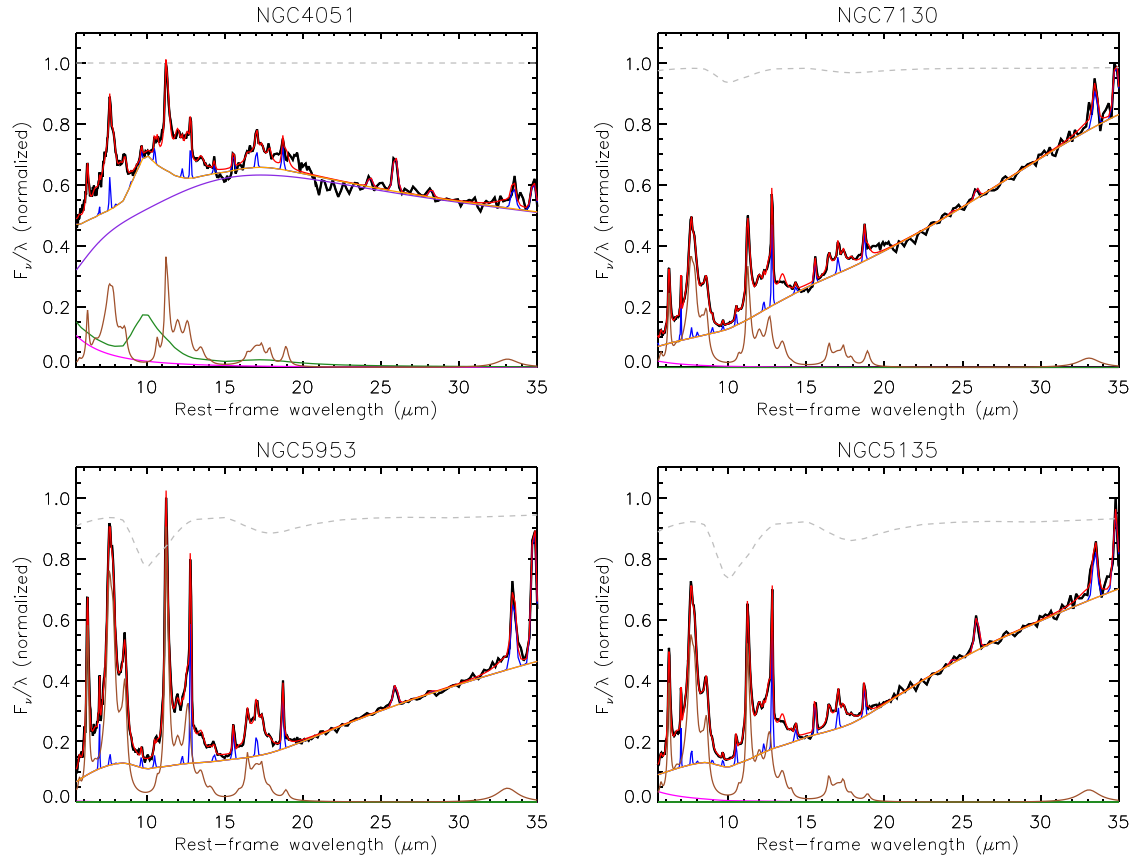
Figure 4. Examples of the MIR spectral modelling using PAHFIT. The Spitzer/IRS rest-frame spectra and model fits correspond to the black and red solid lines. We show the dust continuum (purple solid lines), stellar continuum (pink solid lines), silicate feature in emission (green solid line), and their sum (orange solid line). The grey dashed line indicates the extinction profile. We also show the fitted PAH features (brown solid lines) and emission lines (blue solid lines).

LaMassa et al. 2010; Lyu & Rieke 2018; Alonso-Herrero et al. 2020) by using the same method to extract the PAH feature strengths.

The modified version of PAHFIT employed in this work uses the Ossenkopf, Henning & Mathis (1992) cold dust model for the feature in emission, which peaks at ∼10.1 μm. We use the default model continuum dust temperatures and a stellar continuum component. Since Sy1 galaxies show evidence of the silicates feature in emission or nearly flat in the MIR spectra (see e.g. García-Bernete et al. 2019 and references therein), we use the silicates in emission only for fitting type 1 Seyfert galaxies. Because of the low spatial resolution afforded by Spitzer, the silicate features can produce an additional source of uncertainty in the fitted continuum. The latter can also affect the total measured PAH fluxes. However, we have consistently used the same method for fitting the underlying continuum of all the PAH bands, and thus these effects are mitigated when measuring PAH band ratios. Four sources in our sample (NGC 4388, NGC 5506, NGC 7496, and NGC 7582) show deep silicate absorption that can influence the derived PAH fluxes. We label these sources in all the figures to show that the observed trends are not in any way skewed by the presence of these galaxies. In the future, studies such as this, will benefit from the availability of higher angular resolution spectra for the entire MIR range that will be afforded by the James Webb Space Telescope. Such spectra will help to better constrain the various components of the continuum. Fig. 4 shows examples of the fitting procedure followed, whereas, Appendix B shows the fits for the entire sample. Note that for some AGN-dominated systems in our sample (10/50) PAHFIT does not reproduce the region of the silicate features and, subsequently, we classify those

as unsatisfactory fits of their spectral features (see Table 2 and Appendix B).

Once we subtracted the continuum emission and the emission-line contribution to each MIR spectrum, we obtain the PAH spectrum for each galaxy. In Tables 2 and 3, we list the integrated fluxes and corresponding errors of the MIR PAH features and emission lines, respectively. The list includes, [Ar II] λ6.98, [S IV] λ10.51, [Ne II] λ12.81, [Ne V] λ14.32, [Ne III] λ15.56, [O IV] λ25.91, PAH λ6.2, PAH λ7.7 complex (λ7.42, λ7.60, and λ7.85 features), PAH λ11.3 complex (λ11.23 and λ11.33 features) (all wavelengths given in μm). In the case of the galaxies for which particular emission lines are not detected, we calculated their 3σ upper limits (see Tables 2 and 3).

5 AGN MIR FRACTION

When considering the spatial scales probed by the Spitzer/IRS spectra of the sample galaxies (∼kpc scales), we expect some degree of contribution from the host galaxy to the MIR spectra, in addition to the AGN. To estimate the relative contributions, we use the DEBLENDIRS routine (Hernán-Caballero et al. 2015). This is an IDL routine that decomposes MIR spectra using a linear combination of three spectral components: AGN, PAH, and stellar emission. The combination of components that best reproduce the IRS/Spitzer spectrum is obtained through χ^2 minimization. Subsequently, DE-BLENDIRS estimates the fractional contribution of each component to the total MIR spectrum.

The spectrum of each component is selected from extreme cases of galaxies dominated by AGN, PAH, or stellar emission, using a large

Table 2. Seyfert galaxy PAH measurements with PAHFIT using the Spitzer/IRS spectra. † These galaxies were observed using the staring mode, whereas the remaining galaxies have spectral mapping data. Columns 2–4 correspond to the fluxes and 1σ errors, which are in units of 10^{-14} erg^{-1} cm^{-2}, of the 6.2, 7.7, and 11.3 μm PAH bands. Column 5 indicates the fractional contribution of the AGN component to the MIR spectrum derived from the spectral decomposition of the Spitzer/IRS spectra (see Section 5). Column 6 corresponds to the silicate strength. We note that < corresponds to 3σ upper limits. Sources in italics have unsatisfactory fits of their spectral features and have been ignored from further analysis.

Name	PAH λ6.2 μm	PAH λ7.7 μm (complex)	PAH λ11.3 μm (complex)	AGN MIR contribution (per cent)	S_{Sil}
(1)	(2)	(3)	(4)	(5)	(6)
Mrk 352†	...	...	...	$73 \pm^{18}_{25}$	0.11 ± 0.40
NGC 931	38 ± 2	185 ± 26	63 ± 3	$89 \pm^{5}_{5}$	-0.02 ± 0.16
NGC 1097	86 ± 1	401 ± 8	211 ± 1	$32 \pm^{7}_{8}$	0.11 ± 0.40
NGC 1275	64 ± 2	268 ± 17	167 ± 3	$97 \pm^{2}_{2}$	0.30 ± 0.12
NGC 1365	561 ± 3	2111 ± 37	648 ± 5	$61 \pm^{7}_{10}$	0.16 ± 0.23
ESO 548-G081†	...	...	...	$90 \pm^{10}_{14}$	0.25 ± 0.18
NGC 1566	87 ± 1	333 ± 10	138 ± 2	$49 \pm^{10}_{13}$	0.21 ± 0.25
NGC 1667	29 ± 1	<91	59 ± 1	$19 \pm^{12}_{7}$	-0.28 ± 0.54
MCG-01-13-025†	...	...	...	$93 \pm^{7}_{10}$	0.34 ± 0.19
4U0517+17	56 ± 6	<339	<69	$79 \pm^{6}_{5}$	0.11 ± 0.26
ESO 362-G018	47 ± 2	194 ± 17	81 ± 2	$79 \pm^{5}_{13}$	0.22 ± 0.19
UGC 3478†	39 ± 3	<157	61 ± 7	$71 \pm^{10}_{13}$	0.13 ± 0.27
Mrk 6	23 ± 2	123 ± 26	53 ± 2	$88 \pm^{9}_{10}$	0.15 ± 0.17
Mrk 79	24 ± 2	<155	45 ± 3	$91 \pm^{6}_{8}$	0.14 ± 0.17
NGC 2992	144 ± 2	660 ± 23	197 ± 3	$71 \pm^{9}_{7}$	0.07 ± 0.23
NGC 3227	332 ± 13	1695 ± 124	423 ± 42	$53 \pm^{10}_{11}$	0.00 ± 0.28
NGC 3516	20 ± 2	<98	45 ± 3	$95 \pm^{5}_{9}$	0.13 ± 0.18
NGC 3783†	...	...	...	$73 \pm^{11}_{4}$	0.15 ± 0.24
NGC 3786†	72 ± 2	<232	109 ± 4	$42 \pm^{12}_{10}$	-0.09 ± 0.30
UGC 6728†	...	...	...	$97 \pm^{3}_{13}$	0.15 ± 0.24
NGC 3982	28 ± 1	148 ± 11	50 ± 1	$40 \pm^{10}_{10}$	0.06 ± 0.26
NGC 4051	97 ± 3	552 ± 30	188 ± 4	$80 \pm^{6}_{7}$	0.22 ± 0.15
NGC 4138	18 ± 1	<58	47 ± 1	$37 \pm^{10}_{10}$	0.18 ± 0.26
NGC 4151	...	...	...	$97 \pm^{3}_{6}$	0.08 ± 0.17
NGC 4235†	...	...	...	$77 \pm^{17}_{23}$	0.05 ± 0.43
NGC 4253	86 ± 2	495 ± 27	115 ± 3	$87 \pm^{5}_{9}$	0.08 ± 0.20
NGC 4388	105 ± 6	<975	191 ± 6	$65 \pm^{7}_{6}$	-0.67 ± 0.16
NGC 4395†	2 ± 1	<37	4 ± 1	$61 \pm^{15}_{11}$	-0.39 ± 0.26
NGC 4501	10 ± 1	37 ± 2	40 ± 1	$8 \pm^{6}_{6}$	-0.32 ± 0.68
NGC 4593	31 ± 2	180 ± 28	77 ± 3	$91 \pm^{4}_{9}$	0.26 ± 0.14
NGC 4639†	7 ± 1	<24	17 ± 1	$35 \pm^{18}_{16}$	-0.18 ± 0.65
ESO 323-G77†	170 ± 16	<734	247 ± 28	$69 \pm^{11}_{11}$	0.10 ± 0.24
NGC 5033	58 ± 1	248 ± 10	156 ± 1	$14 \pm^{9}_{6}$	-0.36 ± 0.75
NGC 5135	519 ± 1	2187 ± 15	591 ± 2	$14 \pm^{10}_{11}$	-0.44 ± 0.76
MCG-06-30-015	32 ± 2	<192	70 ± 3	$94 \pm^{5}_{7}$	0.21 ± 0.15
IC 4329A	...	...	...	$92 \pm^{7}_{9}$	0.15 ± 0.18
NGC 5347	35 ± 2	<234	76 ± 3	$83 \pm^{8}_{7}$	0.13 ± 0.21
NGC 5506	242 ± 3	<2897	396 ± 5	$60 \pm^{9}_{8}$	-0.98 ± 0.29
NGC 5548	27 ± 2	121 ± 20	54 ± 3	$88 \pm^{4}_{3}$	0.24 ± 0.15
NGC 5953	253 ± 1	905 ± 19	326 ± 3	$9 \pm^{8}_{5}$	-0.29 ± 0.69
IRAS 18325-5926†	113 ± 8	698 ± 83	180 ± 15	$67 \pm^{8}_{8}$	-0.13 ± 0.21
NGC 6814†	...	...	...	$83 \pm^{10}_{13}$	0.13 ± 0.24
NGC 6860	...	...	...	$82 \pm^{10}_{12}$	0.19 ± 0.16
NGC 6890	36 ± 2	<175	62 ± 2	$82 \pm^{5}_{6}$	0.23 ± 0.16
NGC 7130	236 ± 1	1096 ± 9	296 ± 13	$45 \pm^{9}_{9}$	-0.21 ± 0.42
NGC 7314†	21 ± 5	<129	<64	$84 \pm^{5}_{8}$	-0.34 ± 0.29
NGC 7469	834 ± 3	3181 ± 47	844 ± 6	$45 \pm^{9}_{7}$	0.10 ± 0.28
NGC 7496	189 ± 3	646 ± 32	196 ± 5	$39 \pm^{4}_{4}$	-0.41 ± 0.28
NGC 7582	1382 ± 2	6641 ± 51	1258 ± 5	$25 \pm^{9}_{9}$	-1.00 ± 0.41
NGC 7590	32 ± 1	125 ± 11	49 ± 1	$14 \pm^{11}_{11}$	-0.32 ± 0.73

Table 3. Seyfert galaxy emission line measurements with PAHFIT using the Spitzer/IRS spectra. † These galaxies were observed using the staring mode, whereas the remaining galaxies have spectral mapping data. The fluxes and 1σ errors are in units of 10^{-15} erg^{-1} cm^{-2}. We note that $<$ corresponds to 3σ upper limits. Sources in italics have unsatisfactory fits of their spectral features and have been ignored from further analysis.

Name	[Ar II] λ6.99	[S IV] λ10.51	[Ne II] λ12.81	[Ne V] λ14.32	[Ne III] λ15.56	[O IV] λ25.89
E_{ion} (eV)	15.8	34.8	21.6	97.1	41.0	54.9
Mrk 352†	...	...	...	...	...	...
NGC 931	<19.3	156.3 ± 5.4	38.6 ± 3.5	78.1 ± 12.1	111.2 ± 6.2	287.7 ± 7.3
NGC 1097	<0.9	36.5 ± 1.7	15.9 ± 1.5	<44.4	17.4 ± 3.3	31.6 ± 6.4
NGC 1275	113.6 ± 4.2	114.7 ± 4.7	348.1 ± 3.2	<8.7	149.9 ± 6.6	29.1 ± 7.6
NGC 1365	286.0 ± 6.7	208.6 ± 7.3	820.6 ± 5.4	<209.7	157.9 ± 13.3	672.1 ± 17.4
ESO 548-G081†	...	...	...	...	...	...
NGC 1566	33.2 ± 1.9	30.1 ± 1.8	84.2 ± 1.4	<29.2	<59.0	<79.8
NGC 1667	39.9 ± 2.2	18.7 ± 2.2	75.5 ± 1.8	<45.5	3.3 ± 4.2	23.1 ± 7.1
MCG-01-13-025†	...	...	...	...	...	...
4U0517+17	52.4 ± 16.6	135.6 ± 32.6	126.8 ± 32.2	75.9 ± 10.2	141.8 ± 5.8	269.9 ± 13.0
ESO 362-G018	11.7 ± 3.1	38.6 ± 3.2	64.9 ± 2.2	<19.8	39.1 ± 5.2	73.2 ± 6.0
UGC 3478†	<65.7	92.1 ± 9.9	77.3 ± 8.5	87.8 ± 6.6	127.5 ± 6.4	402.9 ± 2.8
Mrk 6	73.9 ± 4.1	161.4 ± 4.6	179.0 ± 3.3	<43.5	262.2 ± 4.5	253.1 ± 5.1
Mrk 79	45.6 ± 4.4	116.6 ± 5.0	60.2 ± 3.3	60.3 ± 13.7	135.2 ± 5.1	304.6 ± 6.3
NGC 2992	161.9 ± 5.0	255.3 ± 5.6	376.2 ± 4.0	107.9 ± 15.2	377.8 ± 7.4	660.6 ± 8.7
NGC 3227	252.2 ± 37.7	245.0 ± 43.1	613.1 ± 61.8	158.0 ± 20.0	430.8 ± 8.4	480.0 ± 9.1
NGC 3516	14.9 ± 4.4	127.5 ± 5.4	46.3 ± 3.3	41.9 ± 11.8	116.1 ± 6.0	402.5 ± 6.3
NGC 3783†	...	...	...	...	...	...
NGC 3786†	50.8 ± 5.3	56.0 ± 6.1	118.9 ± 5.0	<124.6	106.2 ± 4.3	132.1 ± 2.4
UGC 6728†	...	...	...	...	...	...
NGC 3982	14.2 ± 2.6	24.5 ± 2.5	72.7 ± 1.9	<40.8	24.4 ± 3.9	<34.0
NGC 4051	31.3 ± 5.8	59.7 ± 6.5	124.8 ± 4.2	<84.9	64.16 ± 6.4	218.4 ± 7.2
NGC 4138	15.6 ± 2.7	11.1 ± 1.2	35.9 ± 1.1	<8.2	32.6 ± 1.4	30.2 ± 2.5
NGC 4151	...	...	...	...	...	...
NGC 4235†	...	...	...	...	...	...
NGC 4253	51.0 ± 4.6	147.8 ± 5.3	162.2 ± 3.7	78.7 ± 13.9	116.9 ± 8.1	302.6 ± 8.0
NGC 4388	243.3 ± 6.0	577.5 ± 6.8	569.2 ± 4.5	458.7 ± 20.4	925.6 ± 15.9	2473.0 ± 11.3
NGC 4395†	12.5 ± 2.1	20.8 ± 2.7	36.3 ± 3.1	13.5 ± 1.3	28.7 ± 0.6	18.1 ± 2.4
NGC 4501	19.8 ± 0.4	6.9 ± 0.4	40.5 ± 0.3	<5.0	14.0 ± 0.8	8.6 ± 1.5
NGC 4593	<26.5	47.6 ± 5.7	46.1 ± 3.6	<50.9	31.6 ± 7.0	120.8 ± 7.4
NGC 4639†	<7.8	<7.3	10.3 ± 1.5	<6.7	4.6 ± 1.2	<4.3
ESO 323-G77†	<144.1	122.1 ± 32.0	249.1 ± 26.5	<237.3	156.4 ± 14.6	290.7 ± 30.1
NGC 5033	45.8 ± 1.8	18.2 ± 1.8	151.2 ± 1.5	11.6 ± 2.9	41.5 ± 1.2	41.3 ± 2.1
NGC 5135	354.7 ± 2.1	219.9 ± 2.7	1006.0 ± 1.9	137.3 ± 8.8	346.5 ± 2.9	455.8 ± 5.0
MCG-06-30-015	19.4 ± 5.0	98.1 ± 5.4	35.1 ± 3.3	<70.9	<40.2	131.5 ± 6.6
IC 4329A	...	...	...	...	...	...
NGC 5347	27.1 ± 4.1	56.9 ± 4.4	45.8 ± 3.0	<61.3	<12.5	47.2 ± 6.5
NGC 5506	340.6 ± 7.6	804.4 ± 8.5	706.5 ± 6.4	494.9 ± 22.9	845.1 ± 9.7	2069.0 ± 11.3
NGC 5548	27.0 ± 4.1	32.0 ± 4.2	59.0 ± 3.3	<47.5	46.2 ± 5.5	58.7 ± 6.6
NGC 5953	127.3 ± 3.7	40.0 ± 3.5	437.3 ± 3.5	<62.6	88.8 ± 5.7	84.5 ± 8.1
IRAS 18325–5926†	106.1 ± 35.6	166.5 ± 15.8	359.4 ± 20.3	291.9 ± 13.2	365.2 ± 10.9	450.2 ± 9.0
NGC 6814†	...	...	...	...	...	...
NGC 6860	...	...	...	...	...	...
NGC 6890	14.6 ± 3.4	36.8 ± 3.6	74.5 ± 2.4	<49.4	35.0 ± 5.5	69.3 ± 6.5
NGC 7130	226.6 ± 1.5	94.1 ± 1.5	580.60 ± 1.6	52.0 ± 6.4	166.6 ± 3.8	91.8 ± 4.8
NGC 7314†	<86.9	163.3 ± 30.8	<219.9	178.0 ± 8.3	239.2 ± 5.2	479.1 ± 5.5
NGC 7469	656.8 ± 6.9	226.50 ± 7.5	1569.0 ± 6.8	<85.3	151.6 ± 12.8	278.0 ± 15.0
NGC 7496	106.4 ± 3.8	47.5 ± 3.7	346.2 ± 4.4	<40.1	<31.8	47.5 ± 13.8
NGC 7582	851.6 ± 4.9	388.4 ± 6.4	1956.0 ± 5.2	407.7 ± 34.1	620.4 ± 17.6	1668.0 ± 20.1
NGC 7590	86.4 ± 8.1	<37.7	218.7 ± 6.1	<42.9	16.6 ± 3.7	<26.6

library of Spitzer/IRS spectra. We have consistently avoided the use of the sources themselves as templates, since few of our galaxies are in the AGN library of DEBLENDIRS. Note that we cannot expand the spectral decomposition beyond 22 μm due to limitations in the library. In Table 2, we list the AGN MIR contributions and corresponding errors derived from the spectral decomposition of our sample. The median values of the fractional contribution of the AGN to the MIR Spitzer/IRS spectra for Sy1, Sy1.8/1.9, and Sy2 are 83 ± 17, 61 ± 24, and 25 ± 25, respectively. These estimates are in good agreement with previous works using samples of Sy galaxies (e.g. García-Bernete et al. 2016).

6 PAH EMISSION AND HARDNESS OF THE RADIATION FIELD

The spectral features of the PAH molecules are directly related to their molecular size and structure, charge state, and the radiation field to which the molecules are exposed. Indeed, PAH ratios can

be used as tracers of the size of the PAH molecule (e.g. 6.2/7.7 and 11.3/3.3), the PAH ionization fraction (11.3/7.7 and 11.3/6.2), and the hardness of the radiation field (e.g. 11.3/3.3, 11.3/7.7, and 11.3/6.2) (e.g. Jourdain de Muizon et al. 1990; Draine & Li 2001; Galliano et al. 2008; Sales et al. 2010; Draine et al. 2020; Maragkoudakis et al. 2020; Rigopoulou et al. 2021). In what follows, we infer the hardness of the radiation field based on key observables while we discuss how PAH band ratios enable us to determine the properties of the PAH molecules in Section 7.

Earlier studies have routinely used PAH emission to estimate the SFR in the circumnuclear regions of AGN (see e.g. Diamond-Stanic & Rieke 2012; Esquej et al. 2014). However, limited knowledge of the effect of the radiation field on these molecules is a shortcoming of this approach. Often, AGN-dominated systems do not show strong PAH features in their nuclear IR spectra. Even in AGN that show these features, they often have low equivalent width compared to those observed in star-forming galaxies. Therefore, it has been proposed that PAH molecules are destroyed by the very hard radiation field of the AGN (e.g. Aitken & Roche 1985; Roche et al. 1991; Voit 1992; Siebenmorgen et al. 2004) or that these features are diluted by the strong AGN continuum (e.g. Alonso-Herrero et al. 2014; Ramos Almeida et al. 2014; García-Bernete et al. 2015). However, other studies did not find dilution on the 11.3 μm feature using radial profiles of subarcsecond resolution spectra (Esparza-Arredondo et al. 2018). In addition, AGN-dominated systems that show PAH features could be explained by a shielding effect of the PAH due to H_2 molecules when the column density is high (e.g. Aitken & Roche 1985; Voit 1992; Alonso-Herrero et al. 2020) or by AGN excitation of these molecules (e.g. Jensen et al. 2017).

Therefore, it is interesting to investigate the link between PAH emission and the hardness of the radiation field to better understand the effect of very hard radiation fields on PAH molecules which can potentially dramatically influence the PAH properties. With this aim, we compare the relative intensities of the different PAH bands with the hardness of the radiation field of various environments such as powerful AGN, relatively weak AGN, and star-forming galaxies. To do so, we compile IR photometry (IRAS and WISE), together with the MIR spectra, for our sample of AGN and a control sample of star-forming galaxies.

6.1 Dust components and the hardness of the radiation field

The NIR-to-MIR range is well suited to probe the various components of the dust emission produced by the AGN heating. The NIR emission is mainly related to the accretion disc and very hot dust (close to the sublimation temperature; $T_{sub} \sim 2000$ K). The NIR emission also contains the contribution of the stellar emission from the host galaxy, which can be particularly significant in Sy2 galaxies (e.g. Alonso-Herrero, Ward & Kotilainen 1996, Riffel, Rodríguez-Ardila & Pastoriza 2006). On the contrary, the MIR emission comes from warm dust mainly heated by the AGN, but there is also a significant contribution from young stars. These young stars heat the dust in star-forming regions that can even dominate the total MIR emission of galaxies (e.g. Horst et al. 2008; Siebenmorgen et al. 2008).

We use IRAS and WISE colours (e.g. de Grijp, Lub & Miley 1987; Low et al. 1988; Mateos et al. 2012; Stern et al. 2012; Assef et al. 2013), to determine the dust temperature in both of our samples. Powerful heating sources produce warmer IR colours allowing us to distinguish them from cooler sources. We find that $F_{25\ \mu m}/F_{60\ \mu m}$ ratio is even better in selecting AGN-dominated systems than the WISE colours according to the AGN contribution to the MIR Spitzer/IRS spectra (see Section 5). Therefore, we use the $F_{25\ \mu m}/F_{60\ \mu m}$ ratio as a proxy for the dust temperature. Note that due to the large IRAS

apertures this ratio is representative of the integrated properties of the galaxies (and may dilute the real impact of the AGN). Thus, we also estimate the AGN contribution to the MIR Spitzer/IRS point-like spectra (see also column 5 of Table 2 in Section 4). See Section 5 for further details on the spectral decomposition.

The hardness of the radiation field can also be traced by MIR fine-structure emission line ratios. The [Ne III]/[Ne II] ratio is used as a robust indicator of the hardness of the radiation field in the surroundings of massive young stars (e.g. Thornley et al. 2000), and in AGN (e.g. Groves, Dopita & Sutherland 2006). However, a recent study reported that [Ne II] emission line can be significantly contaminated by the AGN-dominated systems using a sample of unobscured type 1 AGN (García-Bernete et al. 2017). Because of that, and as a sanity check, we also employ other ionization ratios involving emission lines such as [O IV] and [Ar II] (see Appendix C). Finally, we employ the optical [O III]/[O II] ratio (see Appendix C) which has been known to be a good indicator of the hardness of the radiation field in AGN (e.g. Kewley et al. 2006), although this ratio can be affected by extinction.

6.2 The effect of the hardness of the radiation field to PAH band ratios

In Figs 5 and 6, we present the relationship of the widely used PAH molecular size indicator 6.2/7.7 PAH ratio (e.g. Jourdain de Muizon et al. 1990; Draine & Li 2001; Sales et al. 2010; Draine et al. 2020; Rigopoulou et al. 2021) with the dust temperature (parametrized by $F_{25\ \mu m}/F_{60\ \mu m}$) and the hardness of the radiation field by using the [Ne III]/[Ne II] ratio. We compare the 6.2/7.7 PAH ratio values of Seyfert galaxies to those of the star-forming galaxies in the control sample using the KS test, and, find that they are statistically different (see Table 4). The same holds when using LIRGs or H II galaxies instead of the entire star-forming control sample. However, the 6.2/7.7 PAH ratio values of those sources classified as AGN/SF composite (based on their UV emission and/or emission line ratios; see Table 1) and the star-forming galaxies in the control sample are similar according to the KS test, since the null hypothesis cannot be rejected (see Table 4). In general, we find larger values of the 6.2/7.7 PAH ratio for harder radiation fields in star-forming galaxies compared with AGN-dominated systems. We also find that AGN show a gradual decrease in the 6.2/7.7 PAH ratio with harder radiation fields, whereas the control sample of star-forming galaxies shows a marked increase of this ratio with the hardness of the radiation field (see black dashed lines in Figs 5 and 6 and Table 5). We discuss this issue further in Section 7.

In the case of the 11.3/3.3 PAH ratio, star-forming galaxies in the control sample have comparable 11.3/3.3 PAH ratios to the AGN sample (see Figs 7 and 8). Indeed, the 11.3/3.3 PAH ratio distributions of AGN and star-forming galaxies are similar according to the KS test (see Table 4). For the control sample of star-forming galaxies, we did not find a strong relationship between the 11.3/3.3 PAH ratio and the dust temperature of the galaxy (see left-hand panel of Fig. 7 and Table 5). However, we find that the harder the radiation field (traced by the [Ne II] or [Ne III]) the lower the 11.3/3.3 PAH ratio (see left-hand panel of Fig. 8 and Table 5).

These findings are in agreement with the results reported by Mori et al. (2012). They showed that the 11.3/3.3 PAH ratio is mostly controlled by the incident radiation field in molecular clouds and photodissociation regions in the Large Magellanic Cloud. This also confirms the predicted enhancement of the 3.3 μm PAH band compare with other PAH bands with the increase of the hardness of the radiation field by theoretical models (Rigopoulou et al. 2021).
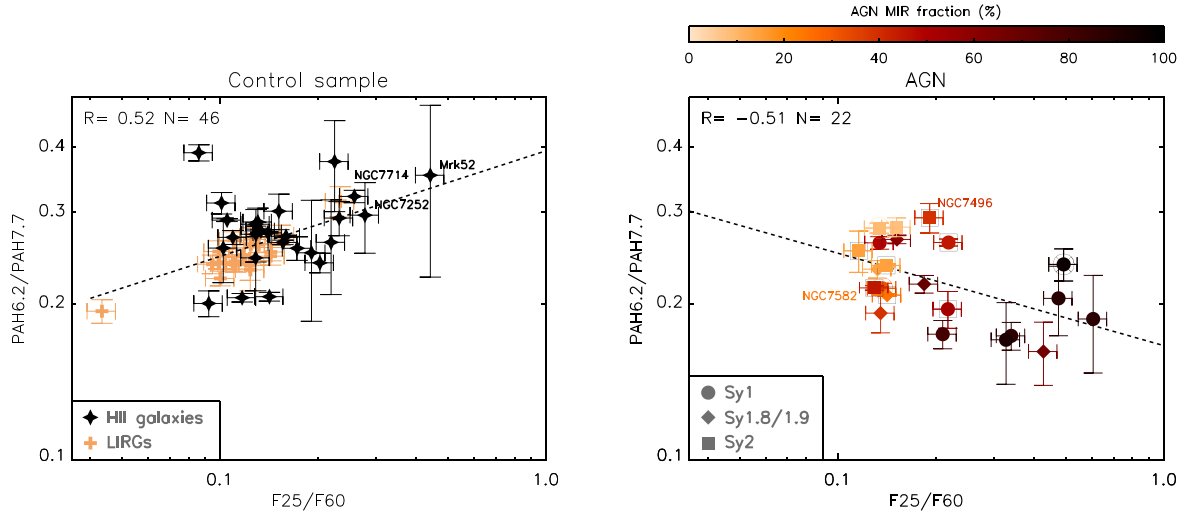
Figure 5. 6.2/7.7 PAH ratio versus $F_{25\,\mu m}/F_{60\,\mu m}$ IRAS colour for those sources with measured PAH fluxes. Left-hand panel: control sample of star-forming galaxies. Black stars and brown crosses correspond to H II galaxies and LIRGs. Right-hand panel: Seyfert galaxies. Filled circles, diamond, and squares correspond to Sy1, Sy1.8/1.9, and Sy2, respectively. Note that open squares and circles represent galaxies that have been also classified as AGN/SF composite and LINER, respectively. The black dashed lines in both panels are linear fits (see Table 5). Labelled sources correspond to Seyfert galaxies with deep silicates in absorption.
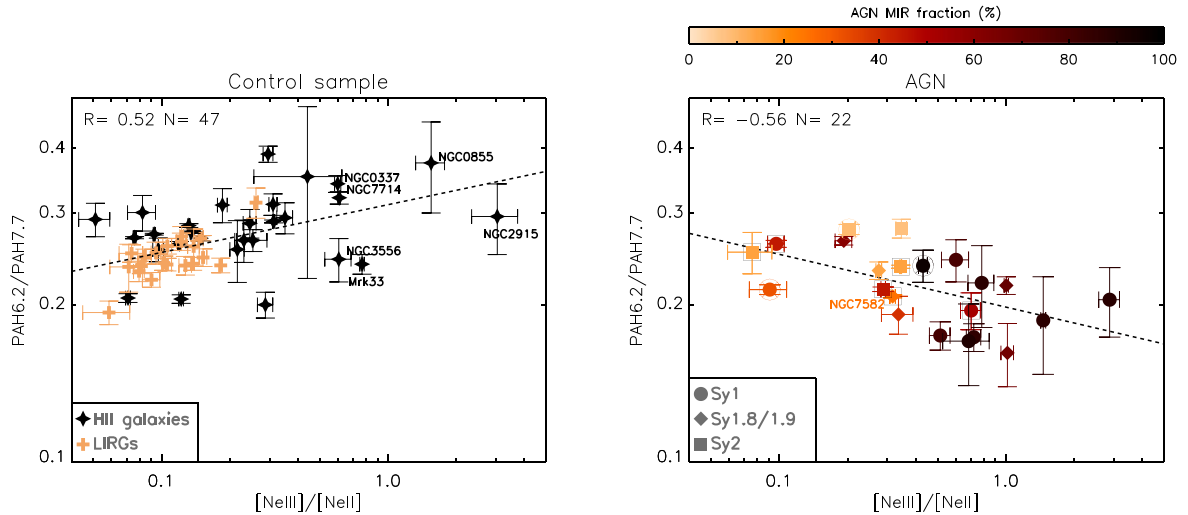
Figure 6. Same as Fig. 5 but using the [Ne III]/[Ne II] ratio instead of the $F_{25\,\mu m}/F_{60\,\mu m}$ ratio.

On the other hand, for the AGN sample we find an almost flat relation between the 11.3/3.3 and the [NeIII]/[NeII] ratio (see right-hand panel of Figs 7, 8, and C1 in Appendix C, but also Section 7 for more details on this). It is worth noting that only a small fraction of the Sy galaxies in our sample have measurements of the PAH $\lambda 3.3\ \mu m$ feature. Furthermore, the mixture of instruments (with different sensitivities), together with the different extinction level for 3.3 and 11.3 μm can be also significantly affecting this ratio.

We next examine whether there is any relationship of PAH ratios related to the ionization fraction of the molecules such as 11.3/7.7 and 11.3/6.2 (e.g. Draine & Li 2001; Galliano et al. 2008; Draine et al. 2020; Rigopoulou et al. 2021) with the dust temperature ($F_{25\,\mu m}/F_{60\,\mu m}$; see Fig. 9) and the [Ne III]/[Ne II] ratio (see Fig. 10). Using the KS test and comparing the 11.3/7.7 and 11.3/6.2 PAH ratio distributions of both samples, we find statistically significant differences between Seyfert and star-forming galaxies (see Table 4). These differences persist when using LIRGs or H II galaxies only

instead of the entire star-forming control sample. In contrast, the 11.3/7.7 and 11.3/6.2 PAH ratio distributions of star-forming galaxies and those sources classified as AGN/SF composite are similar according to the KS test (see Table 4). We also find that the 11.3/7.7 and 11.3/6.2 PAH ratios show similar trends, but there is more scatter when using the 7.7 μm PAH band. This is related to the fact that this PAH band complex consisting of the 7.42, 7.60, and 7.85 μm features results in an upper limit due to the low detection rate of the 7.42 μm in a significant part of our sample (see Section 4). Therefore, hereafter we discuss only the trends found for 11.3/6.2.

Figs 9 and 10 show that Sy galaxies with relatively low contribution of the AGN (<40 per cent) have a large scatter for this ratio. However, those sources classified as AGN/SF composites are found in the region where the star-forming galaxies of the control sample are located. In contrast, the 11.3/6.2 values of galaxies in the control sample are more concentrated around ~ 0.7–1.4 indicating that in star-forming galaxies this ratio does not depend on the dust
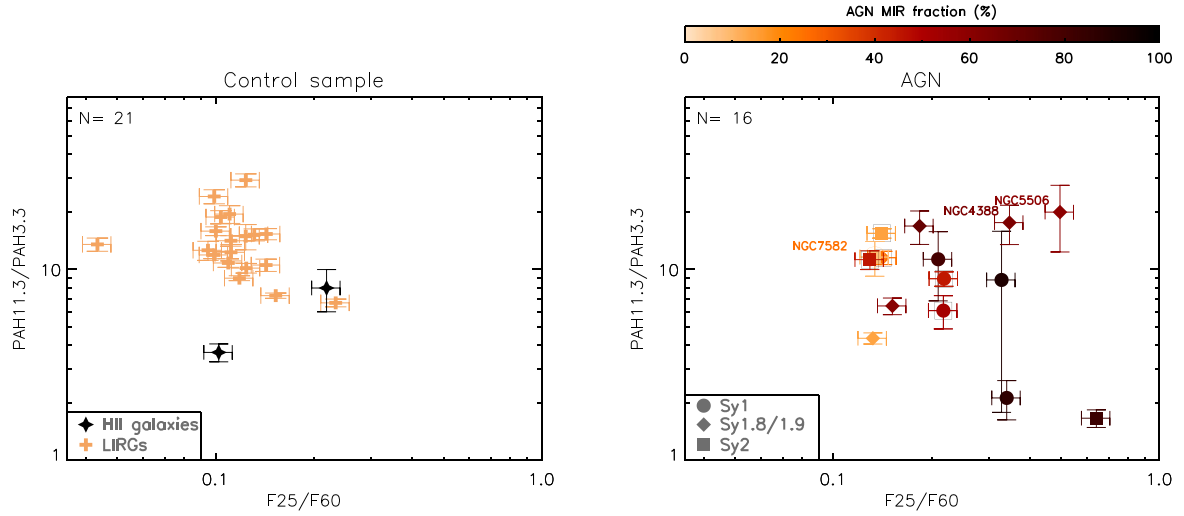
Figure 7. 11.3/3.3 PAH ratio versus $F_{25\,\mu m}/F_{60\,\mu m}$ IRAS colour for those sources with measured PAH fluxes. Left-hand panel: control sample of star-forming galaxies. Black stars and brown crosses correspond to H II galaxies and LIRGs. Right-hand panel: Seyfert galaxies. Filled circles, diamond, and squares correspond with Sy1, Sy1.8/1.9, and Sy2, respectively. Note that open squares and circles represent galaxies that have been also classified as AGN/SF composite and LINER, respectively. Labelled sources correspond to Seyfert galaxies with deep silicates in absorption.
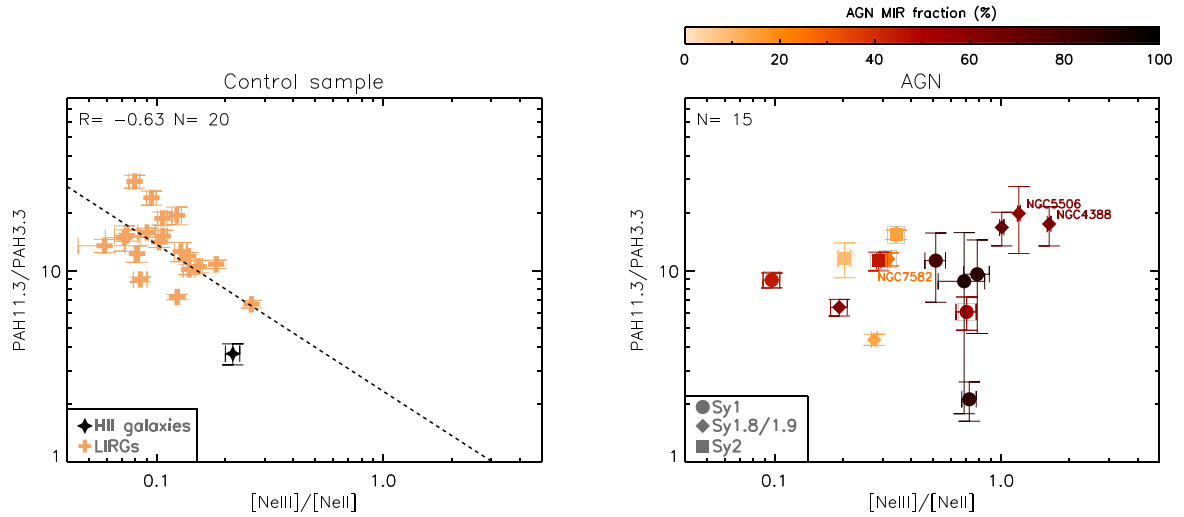
Figure 8. Same as Fig. 7 but using the [Ne III]/[Ne II] ratio instead of the $F_{25\,\mu m}/F_{60\,\mu m}$ ratio. The black dashed line in the left-hand panel is a linear fit (see Table 5).

temperature (see left-hand panel of Fig. 9) or the hardness of the radiation field as traced by the [Ne II] or [Ne III] ratio (see left-hand panel of Fig. 10). It is worth stressing that our findings are independent of the use of an IR or optical indicator for the hardness of the radiation field (see Fig. C1 in Appendix C). This result is in agreement with those reported by Brandl et al. (2006) and Smith et al. (2007a) using star-forming galaxies.

We also find that AGN dominated systems have an average 11.3/6.2 PAH ratio (∼2) larger than that of the star-forming galaxies (average 11.3/6.2 PAH ratio ∼1; see Figs 9 and 10). The latter is in good agreement with those reported by Smith et al. (2007a) (see also Diamond-Stanic & Rieke 2010; Wu et al. 2010). Smith et al. (2007a) also found larger values of the 11.3/7.7 PAH ratio for weak AGN in comparison with H II galaxies in the SINGs sample. Therefore, using a sample including AGN-dominated systems, this work confirms and extends the result of Smith et al. (2007a) based on the SINGs

galaxies. Smith et al. (2007a) interpreted this as the signature of the small PAH destruction by the hard radiation field of the AGN even in the relatively large aperture probed by Spitzer. Other explanations include, for example, the ionization fraction (see Section 7).

Overall our findings suggest that Sy galaxies with a strong contribution of the AGN have smaller values of 6.2/7.7 PAH ratio and larger values of the 11.3/6.2 PAH ratios (same holds for the 11.3/7.7 PAH ratio but with more scatter). In the case of the 11.3/3.3 PAH ratio, only the galaxies in the control sample show a clear correlation with the hardness of the radiation field.

7 PAH DIAGNOSTIC DIAGRAMS

In this section, we investigate the relative strengths of the PAH bands based on new model grids generated by using theoretically computed PAH spectra based on Density functional theory. We refer the reader
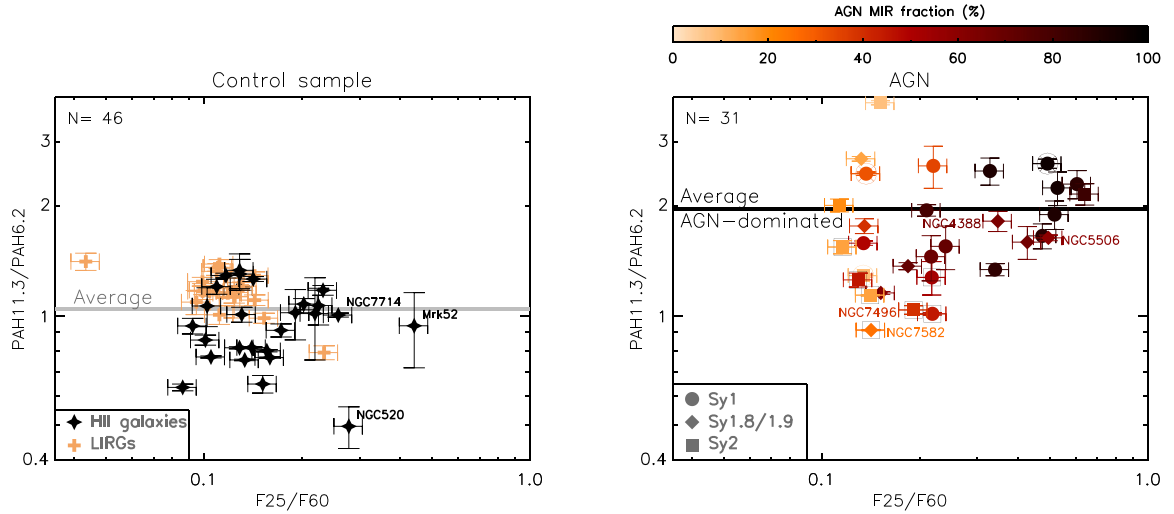
Figure 9. 11.3/6.2 PAH ratio versus $F_{25\,\mu m}/F_{60\,\mu m}$ IRAS colour for those sources with measured PAH fluxes. Left-hand panel: control sample of star-forming galaxies. Black stars and brown crosses correspond to H II galaxies and LIRGs. Right-hand panel: Seyfert galaxies. Filled circles, diamond, and squares correspond with Sy1, Sy1.8/1.9, and Sy2, respectively. Note that open squares and circles represent galaxies that have been also classified as AGN/SF composite and LINER, respectively. The grey and orange horizontal solid lines show the average 11.3/6.2 PAH ratios of star-forming galaxies and AGN-dominated systems (AGN fraction >70 per cent), respectively. Labelled sources correspond to Seyfert galaxies with deep silicates in absorption.
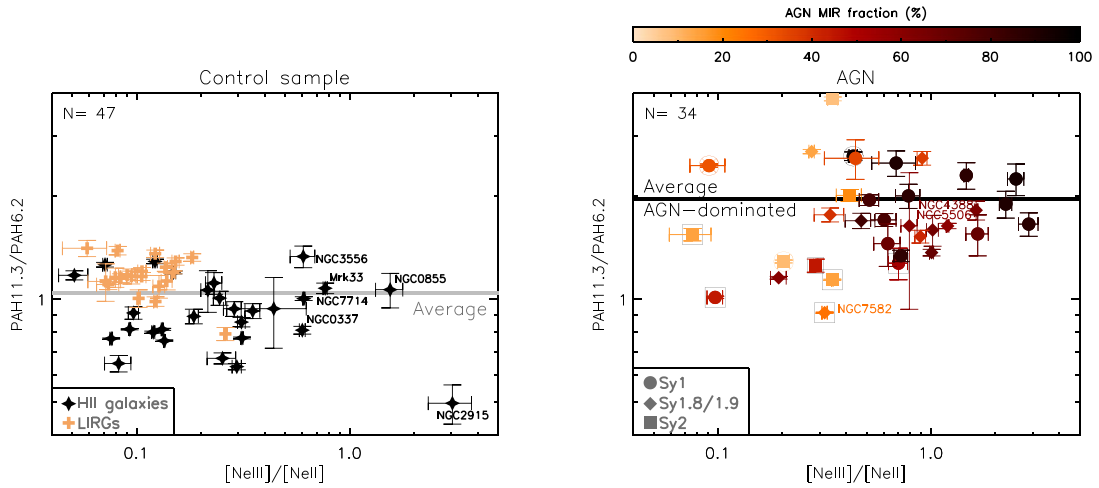
Figure 10. Same as Fig. 9 but using the [Ne III]/[Ne II] ratio instead of the $F_{25\,\mu m}/F_{60\,\mu m}$ ratio.

to Rigopoulou et al. (2021) for more details on how these grids are constructed.

7.1 The 6.2/7.7 versus 11.3/7.7 grid

First we examine the 11.3/7.7 versus 6.2/7.7 PAH ratio diagram for the AGN sample and the control sample of star-forming galaxies studied here. For clarity, in the case of AGN, we exclude objects with upper limits in any of the 6.2, 7.7, and 11.3 μm PAH bands. However, in Appendix D we show those sources with PAH upper limits and note that they generally show the same trend as those sources with detected PAH features.

Fig. 11 shows a large scatter in the values of the measured 6.2/7.7 PAH ratios for the AGN sample suggesting that the mean size of PAHs, and hence the size of the dust grains, differs widely from source to source (compared to the star-forming galaxies). Indeed, weak AGN or those classified as AGN/SF composites tend to cluster

in a narrower part of the diagram closer to the location of star-forming galaxies. Furthermore, most of the measured PAH band ratios in weak AGN and star-forming galaxies are well reproduced by the model grids with PAH molecules showing a ∼70 per cent ionization fraction, medium-to-large molecular size ($100 < N_c < 300$) and exposed to a relatively strong radiation field (see Fig. 11).

Concerning the strength of the AGN, we find that AGN-dominated systems are generally located in the leftmost corner of the grid or even outside of the range of the grid (with measured 6.2/7.7 PAH ratios smaller than 0.25; see Fig. 11 and also Alonso-Herrero et al. 2020). The fact that a fraction of AGN-dominated systems lies beyond the values predicted by the current grid suggests that perhaps larger PAH molecules ($N_c > 400$), are required to reproduce their PAH ratio values. The outcome of the comparison between the observed PAH ratios and the grid suggests that in AGN-dominated systems the PAH emission is consistent with originating in large PAH molecules ($N_c > 300$–400) (see also Figs 5 and 6 in Section 6.2).

Table 4. The KS test probability. In bold we indicate distributions that can be considered as statistically significant different (i.e. p-value < 0.05).

PAH ratio (1)	Samples (2)	D-statistics (3)	p-vaule (4)	Number of sources (5)
6.2/7.7	**AGN versus Control**	0.493	**<0.05**	24 versus 46
6.2/7.7	**AGN versus LIRGs**	0.492	**<0.05**	24 versus 20
6.2/7.7	**AGN versus H II galaxies**	0.554	**<0.05**	24 versus 26
6.2/7.7	AGN/SF comp. versus Control	0.492	0.176	7 versus 46
11.3/7.7	**AGN versus Control**	0.496	**<0.05**	24 versus 46
11.3/7.7	**AGN versus LIRGs**	0.533	**<0.05**	24 versus 20
11.3/7.7	**AGN versus H II galaxies**	0.468	**<0.05**	24 versus 26
11.3/7.7	AGN/SF comp. versus Control	0.193	0.960	7 versus 46
11.3/6.2	**AGN versus Control**	0.734	**<0.05**	38 versus 46
11.3/6.2	**AGN versus LIRGs**	0.737	**<0.05**	38 versus 20
11.3/6.2	**AGN versus H II galaxies**	0.789	**<0.05**	38 versus 26
11.3/6.2	AGN/SF comp. versus Control	0.193	0.960	7 versus 46
11.3/3.3	AGN versus Control	0.349	0.148	18 versus 21
11.3/3.3	AGN/SF comp. versus Control	0.371	0.526	5 versus 21
11.3/7.7 versus 6.2/7.7	**AGN versus Control**	0.586	**<0.05**	24 versus 46
11.3/7.7 versus 6.2/7.7	**AGN versus LIRGs**	0.596	**<0.05**	24 versus 20
11.3/7.7 versus 6.2/7.7	**AGN versus H II galaxies**	0.596	**<0.05**	24 versus 26
11.3/7.7 versus 6.2/7.7	**AGN-dominated versus Control**	0.802	**<0.05**	9 versus 46
11.3/7.7 versus 6.2/7.7	**AGN-dominated versus LIRGs**	0.783	**<0.05**	9 versus 20
11.3/7.7 versus 6.2/7.7	**AGN-dominated versus H II galaxies**	0.868	**<0.05**	9 versus 26
11.3/7.7 versus 6.2/7.7	AGN/SF comp. versus Control	0.365	0.331	7 versus 46
11.3/7.7 versus 6.2/7.7	AGN/SF comp. versus LIRGs	0.364	0.400	7 versus 20
11.3/7.7 versus 6.2/7.7	AGN/SF comp. versus H II galaxies	0.446	0.160	7 versus 26
11.3/7.7 versus 6.2/7.7	**AGN-central versus AGN-extended**	0.627	**<0.05**	15 versus 18
11.3/7.7 versus 11.3/3.3	AGN versus Control	0.417	0.103	14 versus 22

Table 5. Correlation properties. Columns 1 and 2 correspond to the abscissa and ordinate of the linear fit, respectively. Columns 3 and 4 list the samples considered and the number of galaxies included, respectively. Columns 5 and 6 correspond to the Pearson's correlation coefficient (R) and the null probability (p-value). In bold, we indicate fits that can be considered statistically significant (i.e. p-value < 0.05).

X (1)	Y (2)	Sample (3)	N (4)	R (5)	p-value (6)
F25/F60	**PAH6.2/PAH7.7**	**Control**	46	0.52	**<0.05**
F25/F60	**PAH6.2/PAH7.7**	**LIRGs**	20	0.87	**<0.05**
F25/F60	PAH6.2/PAH7.7	H II galaxies	26	0.30	0.130
F25/F60	PAH11.3/PAH3.3	Control	21	−0.30	0.194
F25/F60	PAH11.3/PAH3.3	LIRGs	19	−0.36	0.127
[Ne III]/[Ne II]	**PAH6.2/PAH7.7**	**Control**	46	0.52	**<0.05**
[Ne III]/[Ne II]	**PAH6.2/PAH7.7**	**LIRGs**	20	0.70	**<0.05**
[Ne III]/[Ne II]	PAH6.2/PAH7.7	H II galaxies	26	0.36	0.07
[Ne III]/[Ne II]	**PAH11.3/PAH3.3**	**Control**	20	−0.63	**<0.05**
[Ne III]/[Ne II]	**PAH11.3/PAH3.3**	**LIRGs**	19	−0.53	**<0.05**
F25/F60	**PAH6.2/PAH7.7**	**AGN**	22	−0.51	**<0.05**
[Ne III]/[Ne II]	**PAH6.2/PAH7.7**	**AGN**	22	−0.56	**<0.05**

Following the same method as in Fasano & Franceschini (1987) (see also Peacock 1983), we use a two-dimensional extension of the KS test (hereafter 2-D KS test) to compare the PAH ratio distributions employed in the diagnostic diagrams for the various samples used in this study. We find that the values of the 11.3/7.7–6.2/7.7 PAH ratios for the AGN are different to those of LIRGs and H II galaxies with statistical significance (see Table 4). Note that the difference increases when we use AGN-dominated systems only (see Table 4). However, we find that the 11.3/7.7–6.2/7.7 PAH ratios of sources classified as AGN/SF composites and those of star-forming galaxies are similar according to the 2-D KS test (see Table 4).

Extinction can also have a significant impact on PAH band ratios. This is particularly important for the 11.3μm where this broad PAH feature can be affected by the absorption band (but also emission band in Sy1) from silicate grains which is centred at ∼9.8 μm (e.g. Hernán-Caballero et al. 2020). For instance, NGC 7582, the Seyfert galaxy with the lowest 11.3/7.7 PAH ratio (and also 11.3/6.6 PAH ratio) is also the galaxy with the strongest silicates absorption (S_{sil} ∼ −1.0) that could attenuate the 11.3 μm feature. Nevertheless, the 6.2 to 7.7 μm PAH ratio is less affected by extinction because both bands are relatively close in wavelength and, therefore, their level of extinction is expected to be similar.

Fig. 11 shows that the average 11.3/7.7 PAH ratio of AGN dominated systems is larger than for star-forming galaxies (see also Figs 9 and 10). As discussed in Section 6.2, the previous is more clear for the 11.3/6.2 PAH ratio where the number of upper limits is lower than for the 11.3/7.7 PAH ratio. We remark that the 11.3/7.7 and 11.3/6.2 PAH ratios strongly depend on the ionization fraction but these ratios have a non-negligible dependence on the hardness of the radiation field (Rigopoulou et al. 2021). As expected, we find that AGN-dominated systems have harder radiation fields than star-forming galaxies (see Section 6.2). According to theoretical works (e.g. Rigopoulou et al. 2021), higher values of the 11.3/7.7 and 11.3/6.2 PAH ratios indicate a larger fraction of neutral molecules and/or lower intensity of the underlying radiation field that the PAH molecules are exposed to. Therefore, the relatively high values of the 11.3/7.7 and 11.3/6.2 PAH ratios in AGN-dominated systems suggest larger fractions of neutral PAH molecules compared to star-forming galaxies. This issue is discussed further in Section 7.3.
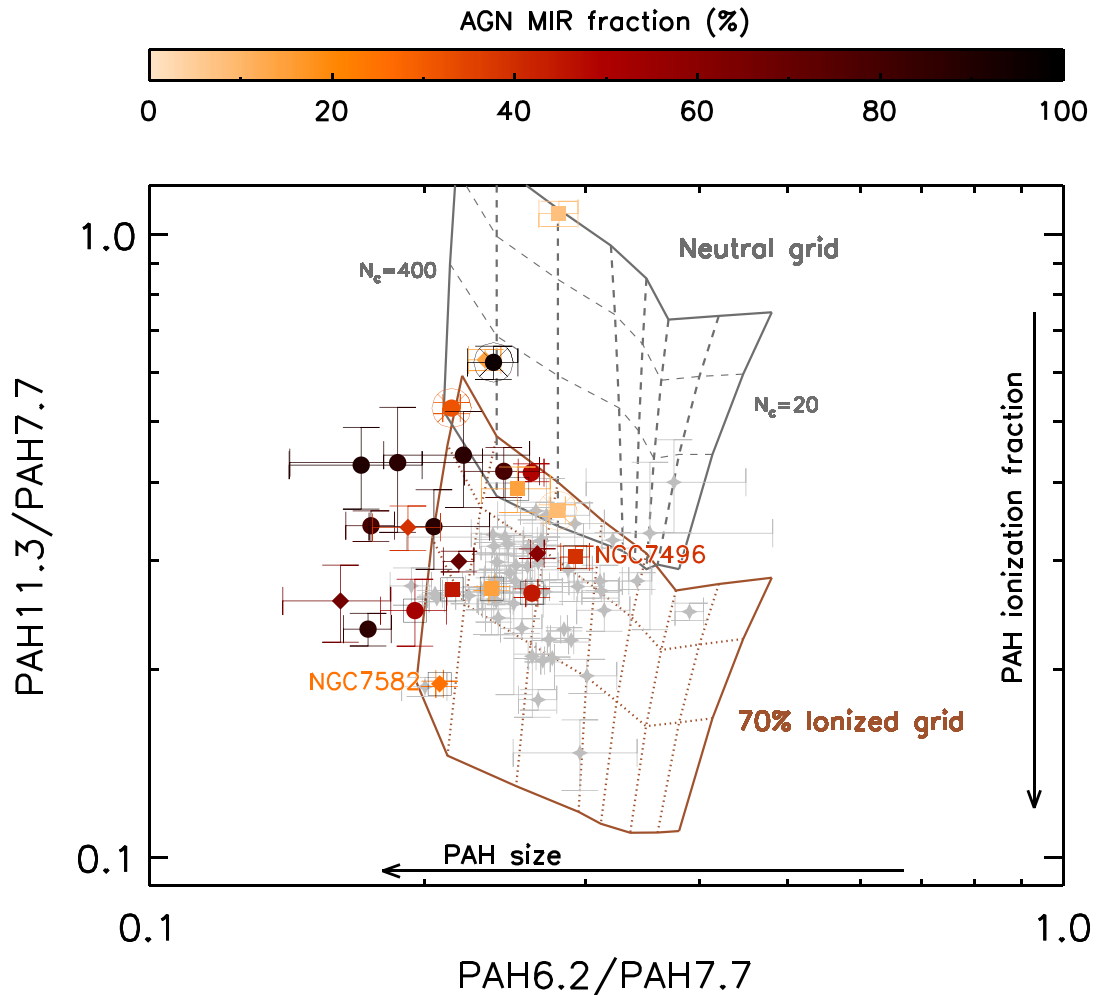
Figure 11. Relative strengths of the 6.2, 7.7, and 11.3 μm PAH features for those AGN with measured PAH fluxes in these bands (24 sources). Filled colour code circles, diamond, and squares correspond with the AGN fraction of Sy1, Sy1.8/1.9, and Sy2, respectively. Note that open squares and circles represent galaxies that have been also classified as AGN/SF composite and LINER, respectively. Grey filled stars correspond to star-forming control sample (46 sources). The grey grid corresponds to neutral PAHs ranging from small PAHs (N_c=20; right side of the grid) to large PAH molecules (N_c=400; left side of the grid). The top and bottom tracks correspond to molecules exposed to a radiation field of ISRF and $10^3 \times$ISRF, respectively. Dashed grey lines correspond to intermediate number of carbons. The brown grid corresponds to a mixture of 70 per cent ionized – 30 per cent neutral PAH molecules exposed to the same radiation fields and for the same number of carbons as in the neutral grid. Dotted brown lines correspond to intermediate number of carbons. Labelled sources correspond to Seyfert galaxies with deep silicates in absorption.

7.2 The 11.3/7.7 versus 11.3/3.3 grid

Maragkoudakis et al. (2020) found that the 11.3 μm and 3.3 μm bands can be used to trace the size of PAH molecules. Rigopoulou et al. (2021) confirmed the use of the 11.3/3.3 PAH ratio as a tracer of PAH size but noted the strong dependence of the 3.3 μm PAH on the intensity of the radiation field (see their fig. 1). Indeed, Rigopoulou et al. (2021) showed that while the peak intensity of all PAH features is dependant on the energy of the photon that is absorbed, the variation in the 11.3/3/3.3 PAH ratio is much higher than that of the 6.2/7.7 PAH ratio. In addition, Mori et al. (2012) investigated molecular clouds and photodissociation regions in the Large Magellanic Cloud[5] and they found that the 11.3/3.3 PAH ratio is a useful tracer for the incident radiation field. This is also in good agreement with our result for the sample of star-forming galaxies,

that the harder the radiation field the lower the 11.3/3.3 PAH ratio (see left-hand panel of Fig. 8).

We next compare the observational data with the 11.3/7.7 versus 11.3/3.3 theoretical grids (see Fig. 12). In agreement with the results presented in Section 7.1, AGN tend to be located in the region of the harder radiation field and larger PAH molecules. We also find that 11.3/3.3–11.3/7.7 distributions of the AGN and control samples are similar according to the 2-D KS test (see Table 4). This is likely due to the similar values of the 11.3/3.3 PAH ratio of AGN compared to those of the star-forming galaxies (see also Section 6.2). In addition, we note that AGN show a relatively flat relation with the various hardness tracers (see Section 6.2). We remark that the 11.3/3.3 PAH can be affected by the hardness of the radiation field (low values for strong radiation fields) but also by the PAH molecular size (high values for large molecules), which could balance this ratio in AGN (see Section 7.3 for further discussion). However, only a small fraction of the Sy galaxies in our sample have PAH λ3.3 μm feature measurements. The results presented here indicate that the 11.3/3.3

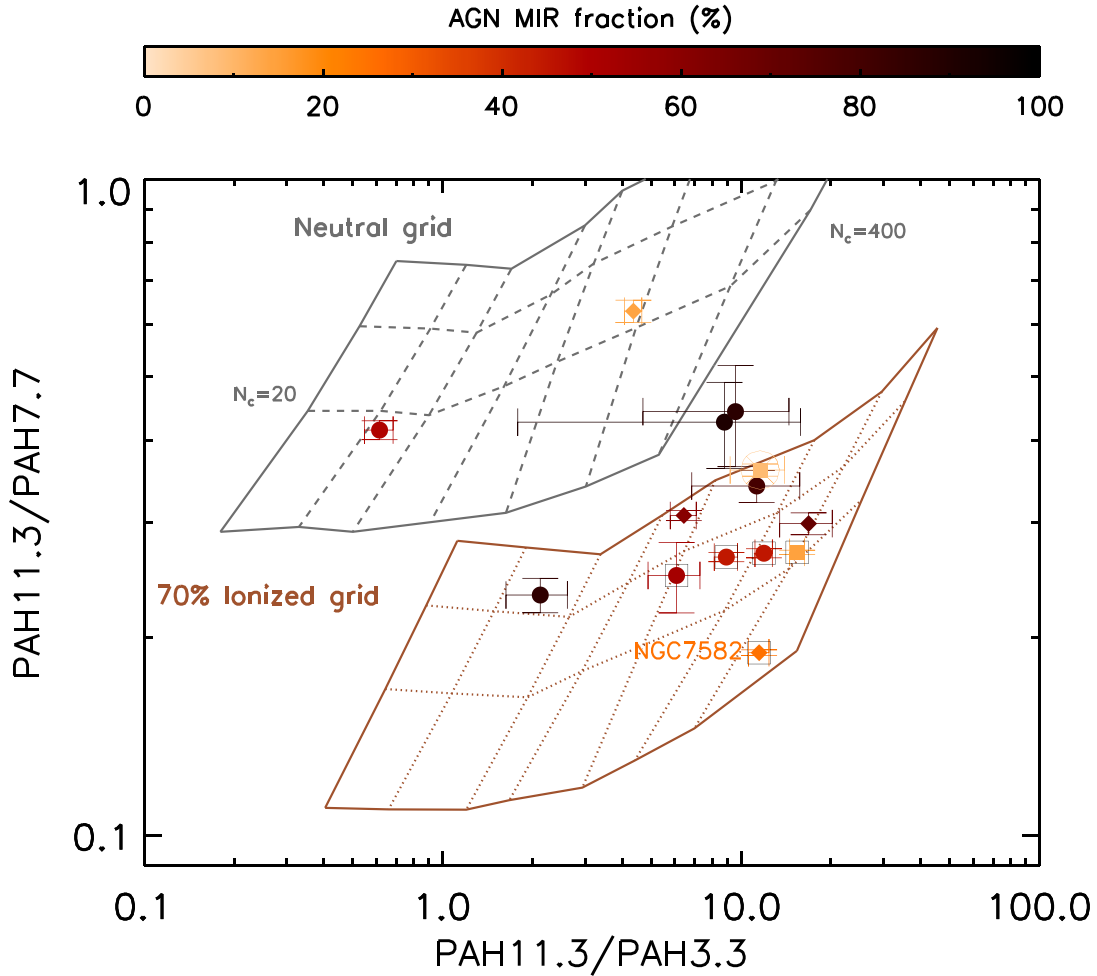[5]Group A targets in Mori et al. (2012) where the destruction of PAHs is expected to be inefficient.

Figure 12. Relative strengths of the 3.3, 7.7, and 11.3 μm PAH features for various astronomical sources with measured PAH fluxes in these bands (14 sources). Filled colour code circles, diamond, and squares correspond with the AGN fraction of Sy1, Sy1.8/1.9, and Sy2, respectively. Note that open squares and circles represent galaxies that have been also classified as AGN/SF composite and LINER, respectively. The grey grid corresponds to neutral PAHs ranging from small PAHs (N_c=20; left side of the grid) to large PAH molecules (N_c=400; right side of the grid). The top and bottom tracks correspond to molecules exposed to a radiation field of ISRF and 10^3 ×ISRF, respectively. Dashed grey lines correspond to intermediate number of carbons. The brown grid corresponds to a mixture of 70 per cent ionized – 30 per cent neutral PAH molecules exposed to the same radiation fields and for the same number of carbons as in the neutral grid. Dotted brown lines correspond to intermediate number of carbons. Note that only a small fraction of the Sy galaxies in our sample have available the PAH λ3.3 μm feature detected. We labelled NGC 7582, one of the galaxies in our sample with a relatively deep silicate feature.

PAH ratio does not vary with the strength of the AGN, but we cannot rule out the possibility that it is due to the mixture of instruments (with different sensitivities) used for measuring the PAH λ3.3 μm fluxes. Note that the different extinction level for 3.3 and 11.3 μm can be also significantly affecting this ratio.

7.3 The 3-D PAH plane

Rigopoulou et al. (2021) presented a 3-D grid by combining the two 2-D diagrams discussed earlier (see also fig. 9 of Rigopoulou et al. 2021) to fully characterize the PAH molecular size, ionization fraction, and hardness of the radiation field.

In Fig. 13, we plot the three PAH band ratios for the samples studied here on the PAH 3-D grid. The plot shows that the measured PAH ratios of H II galaxies, LIRGs, and relatively weak AGN mainly fall in the 70 per cent ionized grid plane (i.e. mixture of 70 per cent ionized – 30 per cent neutral PAH molecules) and intermediate values of the hardness of the radiation field.

From this plot it is clear that the measured PAH ratios of AGN-dominated systems are different to star-forming galaxies and relatively weak AGN. The measured PAH ratios of the former can be explained with a smaller fraction of small PAH molecules, and a smaller fraction of ionized PAHs (see also Sections 6.2 and 7.1). As previously mentioned, the latter is in agreement with previous works using relatively weak AGN (e.g. Smith et al. 2007a; Diamond-Stanic & Rieke 2010).

However, assuming that PAH emission is produced by the UV radiation field, in principle, we would expect a higher ionization fraction for the harder UV radiation field of AGN. A possible explanation for the larger 11.3/7.7 (and 11.3/6.2) PAH ratio in AGN-dominated systems is the variation in the PAH molecular size. This could produce changes of short-wavelength features relative to the 11.3 μm feature (e.g. Draine & Li 2001; Galliano et al. 2008). Alternatively, the 11.3/7.7 (and 11.3/6.2) PAH ratio can also be affected by hydrogenated PAH molecules. Reach et al. (2000) proposed that hydrogenation, which produces an increase in the hydrogen-to-carbon ratio (H/C) in PAH molecules, could explain the extreme
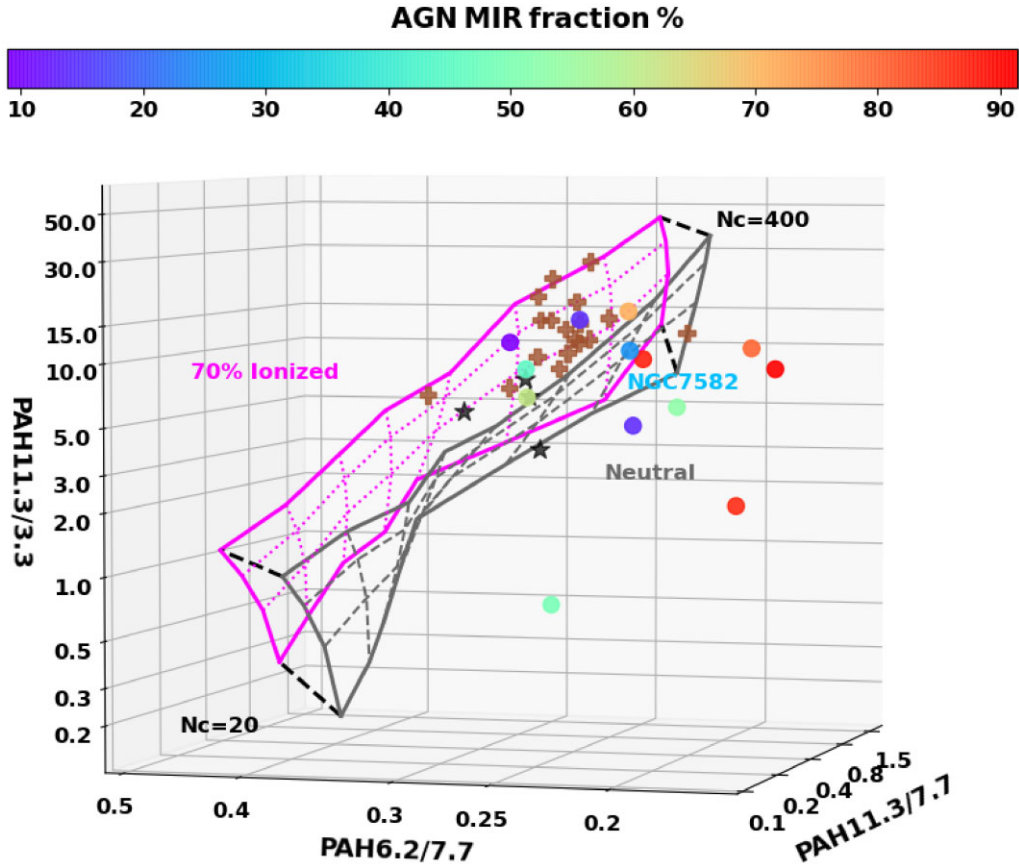
Figure 13. 3-D PAH diagnostic diagram. Relative strengths of the 3.3, 6.2, 7.7, and 11.3 μm PAH features for various astronomical sources with measured PAH fluxes in these bands. Colour code circles correspond to central regions of AGN (14 sources). Black stars and brown crosses represent H II galaxies and LIRGs (22 sources), respectively. The grey grid corresponds to neutral PAHs ranging from small PAHs (N_c=20; left side of the grid) to large PAH molecules (N_c=400; right side of the grid). The top and bottom tracks correspond to molecules exposed to a radiation field of ISRF and 10^3 ×ISRF, respectively. Dashed grey lines correspond to intermediate number of carbons. The magenta grid corresponds to a mixture of 70 per cent ionized – 30 per cent neutral PAH molecules exposed to the same radiation fields and for the same number of carbons as in the neutral grid. Dotted magenta lines correspond to intermediate number of carbons. The solid black line indicates the interception between both grids. Note that only a small fraction of the Sy galaxies in our sample have the PAH λ3.3 μm feature measurements. We labelled NGC 7582, one of the galaxies in our sample with a relatively deep silicate feature.

11.3/7.7 ratios, like the one observed in SMB B1 No 1 (see also Li 2020 for a review). In a forthcoming paper (García-Bernete et al., in prep), we will further investigate how the H/C ratio of PAH molecules affects their band ratios. Finally, the shielding of the PAH molecules by the molecular hydrogen can also be responsible for the increase of neutral species. We discuss this possibility further in Section 7.4.

The results of the comparison with the PAH grid is in good agreement with our findings in Section 6.2. Our findings suggest that AGN-dominated systems generally tend to have a greater fraction of larger molecules, which can be explained by the preferential destruction of small PAH molecules due to X-rays and/or shocks from the AGN (e.g. Voit 1992; Siebenmorgen et al. 2004). However, star-forming galaxies show the opposite trend, the harder the radiation field, the larger the value of the 6.2/7.7 PAH ratio (Figs 5 and 6 in Section 6.2). The trend can be explained by the IP of PAH molecules.[6] Smaller PAH molecules have larger values of the IP (see e.g. Ruiterkamp et al. 2005). Consequently, a relatively harder

environment could produce an enhancement of the 6.2 μm feature with respect to the 7.7 μm PAH in star-forming galaxies (assuming the same PAH molecular size).

We conclude that the presence of an AGN is likely to have a significant impact on the surrounding PAH population by destroying small PAH molecules and favouring large and neutral species. High angular resolution data of the entire ∼3–28 μm range with the James Webb Space Telescope will enable a greater accuracy in the measured PAH ratios (see Section 4) and elucidate the impact of the central AGN in the properties of the PAH molecules located in its vicinity.

7.4 PAH ratios in central and extended AGN regions

As discussed in Section 3, the majority of the Seyfert galaxies in our sample (36/50), were observed in the spectral mapping mode. To further investigate the impact of the AGN on the PAH ratios as a function of distance from the central source, we consider two distinct regions: the central emission and the diffuse/extended emission in the galaxy disc (see Fig. 3; see also Diamond-Stanic & Rieke 2010). The central spectra are extracted assuming a point-like source (see Section 3). For those AGN with extended emission present in the spectral mapping data (i.e. 50 per cent of the sub-sample with spectral mapping mode

[6]Note that the selective destruction of large PAH molecules is an unlikely explanation since large PAH molecules are expected to be more stable (e.g. Allain, Leach & Sedlmayr 1996; Bauschlicher, Peeters & Allamandola 2008 and Murga et al. 2020).
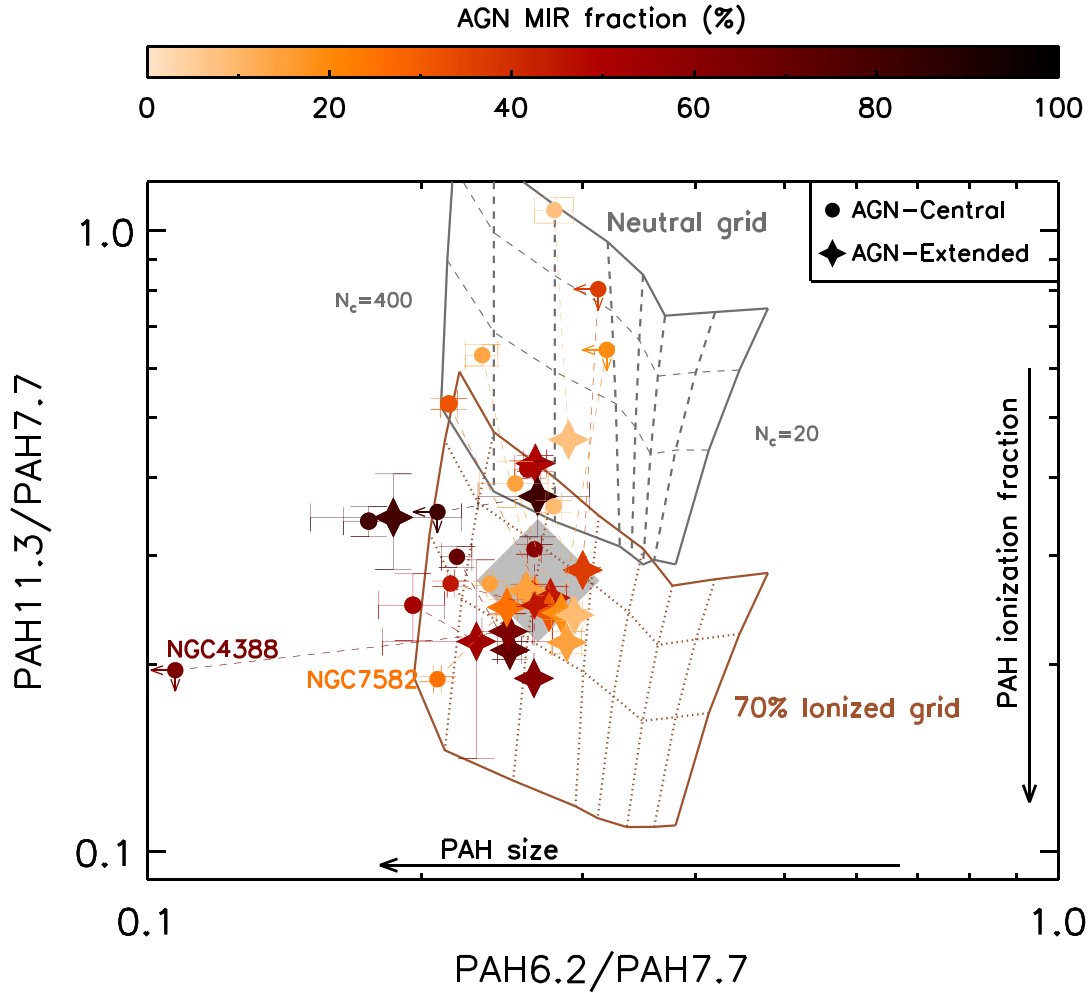
Figure 14. Relative strengths of the 6.2, 7.7, and 11.3 μm PAH features for those AGN with extended emission (18 sources). Colour code symbols indicate the AGN fraction of the source. Filled circles and stars correspond with the circumnuclear and extended emission, respectively. The model grids are the same as in Fig. 11. Labelled sources correspond to Seyfert galaxies with deep silicates in absorption.

observations; 18/36 galaxies), we derive the extended emission spectra. These spectra are computed as the difference between the total minus the central (point-like source) extractions. For comparison, we also apply the same method to 2 LIRGs from our control sample of star-forming galaxies with extended MIR emission (see Fig. 3).

In Fig. 14, we present PAH band ratios for those AGN where it was possible to measure nuclear (central) and extended PAH emission (18 galaxies of the sample). Note that we use the 6.2/7.7 versus 11.3/7.7 grid due to the lack of measurements of the PAH λ3.3 μm for the nuclear/extended regions (see Section 7.2). We also compared the 6.2/7.7–11.3/7.7 PAH ratio distributions of the central and extended regions of Seyfert galaxies using the 2-D KS test and found statistically significant differences between them (see Table 4). The PAH properties in the extended regions (a few kpc scales) of Seyfert galaxies are similar to those seen in star-forming galaxies (see Fig. 14). This is in good agreement with previous works comparing H II galaxies and off-nuclear regions of Seyfert galaxies (e.g. Diamond-Stanic & Rieke 2010). Furthermore, Diamond-Stanic & Rieke (2010) also found larger values of the 11.3/7.7 PAH ratio for AGN in comparison with their off-nuclear regions and H II galaxies. The PAH emission in the central regions of AGN appears to be different, favouring larger and/or more neutral molecules. For the

majority of the galaxies (15/18), the measured PAH ratios in the extended regions of Sys are consistent with PAH ionization fractions of ∼50–70 per cent and smaller PAH sizes.

As previously discussed (see Section 7.3), the destruction of the small PAH molecules can have a significant effect on the 11.3/7.7 PAH ratio. For a given ionization, larger PAH molecules tend to emit more at longer wavelengths therefore large and neutral PAH molecules will produce larger 11.3/7.7 and smaller 6.2/7.7 PAH ratios (e.g. Draine & Li 2001; Li 2020; Rigopoulou et al. 2021). Therefore, PAH molecule destruction could result in an increase of the 11.3/7.7 PAH ratio, but also a change of the number of hydrogens per carbon in PAH molecules (e.g. Li 2020; see also Section 7.3).

The distribution of the molecular hydrogen in AGN is also likely to influence PAH emission. Seyfert galaxies tend to have a large fraction of their molecular gas concentrated toward their centres (e.g. Maiolino et al. 1997). As a result, the molecular gas column density would be smaller at larger distances from the central engine. The lower molecular gas column densities in the extended emission of these galaxies could, therefore, explain the observed increase in the fraction of ionized PAH molecules (e.g. Alonso-Herrero et al. 2020). In contrast, the higher fraction of large and neutral PAHs seen in the central regions of AGN (compared to their extended regions)
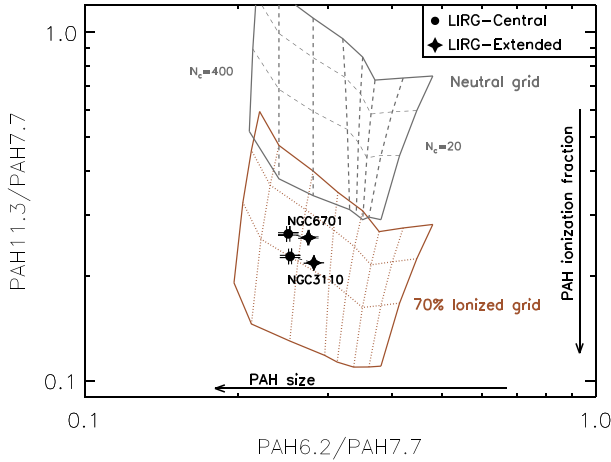
Figure 15. Same as Fig. 14 but for the LIRG galaxies (i.e. NGC 3310 and NGC 6701). The model grids are the same as in Fig. 11.

points to the possible destruction of the smaller PAH molecules by the harsh environments present in the innermost regions of these galaxies. The increase of neutral PAH molecules can be explained by the shielding effect (protection of PAH molecules by the molecular hydrogen present in these regions) due to the large concentration of molecular gas in the centres of Seyfert galaxies as suggested by (e.g. Rigopoulou et al. 2002; Alonso-Herrero et al. 2014, 2020).

For comparison, we also investigate the central and extended PAH ratios of the 2 LIRGs that have no detectable AGN (see Fig. 15). We find rather small variations in their central and extended PAH 6.2/7.7 PAH ratios, but practically the same 11.3/7.7 PAH ratios indicating the same fraction of neutral versus ionized PAH molecules is present in both central and extended regions.

In summary, our findings suggest that the radiation fields of AGN might be altering the molecular size distribution of PAH molecules in their central regions. The changes in the PAH properties due to the presence of the AGN are likely to happen close to the central engine, therefore, high angular observations of the innermost regions of AGN and star-forming galaxies are needed to further investigate this hypothesis.

8 AVERAGED PROPERTIES OF PAH SPECTRAL FEATURES

In this section, we compare *the average PAH band spectra* of AGN, star-forming galaxies (Brandl et al. 2006) and those of local planetary nebulae in the Magellanic Clouds.

For this comparison, we include PNe sources since it is well known that PAH band profiles in these objects vary significantly in comparison with other sources (e.g. Peeters et al. 2002; Shannon & Boersma 2019). In addition, due to the large aperture of Spitzer/IRS, local objects like PNe allow us to better isolate the effects of temperature or metallicity, because are less contaminated by the surrounding medium of the UV source than in galaxies. Therefore, these sources are more likely to show clear changes in the PAH bands for different temperatures/metallicity. By comparing the average PAH spectra, we find that the shape of 11.3μm is similar for PNe, weak AGN (i.e. AGN MIR contribution < 70 per cent) and star-forming galaxies (black, green, and red solid line of Fig. 16, respectively). In contrast, there is a marked difference in the shape and strength of the 7.7 μm PAH complex. In the case of the PNe the feature is narrower and shifted to longer wavelengths in comparison to SF and active galaxies. In a recent study, Shannon & Boersma (2019) found a dependence of the 7.7 μm PAH band peak shift with PAH molecular size, charge, temperature and aliphatic and nitrogen content. However, the origin of the shift is yet unclear.

The shape of the PAH averaged spectra of Seyfert galaxies with relatively low contribution of the AGN (AGN MIR contribution < 70 per cent) and star-forming galaxies are similar. However, although star-forming galaxies have prominent 6.2 and 7.7 μm features, these features appear to be attenuated for both AGN subgroups (AGN MIR contribution < 70 per cent and AGN MIR contribution > 70 per cent). In agreement with the results presented in Section 6, the average PAH spectra of Seyfert galaxies with AGN MIR contribution < 70 per cent and AGN MIR contribution > 70 per cent show noticeable differences: AGN-dominated systems (AGN MIR contribution > 70 per cent; blue solid line of Fig. 16) show broader PAH band profiles than those in weaker ones (AGN MIR contribution < 70 per cent), star-forming galaxies or PNe. Therefore, to reproduce the broad PAH 11.3 μm band profile observed in AGN-dominated systems larger PAH molecules are needed. However, a significant fraction of small and ionized molecules would be necessary to enhance the 6.2 and 7.7 μm PAH bands to reach the same levels as those seen in star-forming galaxies. We refer the reader to Rigopoulou et al. (2021)
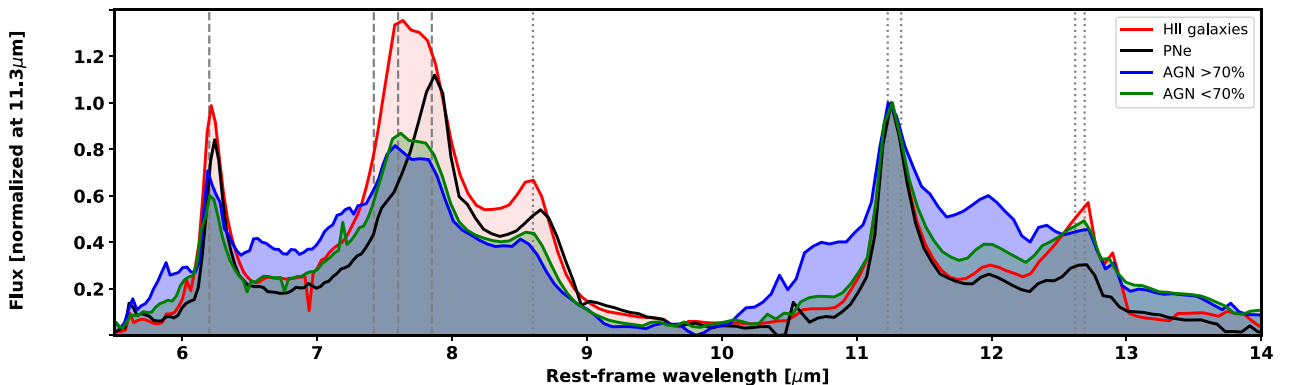

Figure 16. Stacked PAH spectra. The PAH spectra of the various sources fitted in this work. Red, black, blue, and green lines correspond to star-forming galaxies (Brandl et al. 2006), planetary nebula, AGN-dominated Seyfert galaxies (i.e. AGN MIR contribution > 70 per cent) and Seyfert galaxies with a relatively low contribution of the AGN (i.e. AGN MIR contribution < 70 per cent). The grey vertical dashed lines correspond to the most important PAH bands (i.e. 6.2, 7.42, 7.60, 7.85, 8.61, 11.23, 11.33, 12.62, and 12.69 μm features).

for further details on the theoretical PAH profiles. Summarizing, the outcome of the comparisons of the averaged PAH spectra of various sources is in agreement with the findings from our earlier analysis presented in Section 7.

9 CONCLUSIONS

Using a sample of Seyfert galaxies (50 galaxies; $D_L < 100$ Mpc), we investigated the PAH emission originating in the central region of the AGN and compared the results with a control sample of star-forming galaxies (22 LIRGs and 30 H II galaxies). In addition, we studied the difference between the central and extended PAH properties. To do so, we used newly developed PAH diagnostic grids derived from theoretical spectra. This allows disentangling between properties of the PAH molecules such as the size, ionization fraction and hardness of the underlying radiation field. We compared the predicted and observed PAH ratios using Spitzer/IRS IR spectral data for the sample of Seyfert galaxies and a control sample of star-forming galaxies. The main results are as follows.

(i) Hardness of the radiation field. In agreement with theoretical predictions, we find that non-AGN sources have larger 11.3/3.3 PAH ratios for softer radiation fields as traced by the [Ne II] or [Ne III] ratio. In contrast, AGN tend to have a flat relation between 11.3/3.3 PAH ratios and the hardness of the radiation field. In general, we measure larger values of the 6.2/7.7 PAH ratio for harder radiation fields in star-forming galaxies compared with AGN-dominated systems.

(ii) PAH molecular size. We find that the 6.2/7.7 PAH ratio values of Seyfert galaxies and the star-forming galaxies are statistically different. In general, the measured 6.2/7.7 PAH ratio of AGN-dominated systems are smaller than those of star-forming galaxies. A fraction of these AGN-dominated systems lies beyond the range predicted by the grid suggesting that their PAH ratios would require the presence of large PAH molecules ($N_c > 400$).

(iii) PAH Ionization fraction. AGN-dominated systems have a higher average 11.3/6.2 (and 11.3/7.7) than star-forming galaxies. This indicates a larger fraction of neutral PAH molecules in AGN-dominated systems compared with the control sample of star-forming galaxies. This suggests that the nuclear molecular gas concentrated in AGN centres could be playing a role in protecting their nuclear PAH molecules (shielding), or that ionized PAH molecules can be destroyed more easily than neutral ones in hard environments.

(iv) Weak AGN or sources classified as AGN/SF composites and star-forming galaxies tend to cluster in a narrow part of 11.7/7.7 versus 6.2/7.7 diagram. In general, they are well reproduced by the model grids with PAH molecules with ∼70 per cent ionization fraction, medium-to-large molecular size ($100 < N_c < 300$) and exposed to a relatively strong radiation field ($>$ ISRF).

(v) We find that in the extended emission of AGN, the PAH ratios are closer to star-forming galaxies than their central regions. The measured PAH ratios of the extended emission of Seyfert galaxies can be explained with larger fractions of ionized and small PAH molecules than in their nuclear regions.

(vi) We find tentative evidence that Seyfert-like AGN-dominated systems can introduce changes in the PAH population that are significant even on kpc scales. This is particularly important for AGN-dominated systems which could potentially be responsible for the destruction of small PAH molecules, and affect the emission of large and neutral ones. Therefore, caution must be applied when using PAH bands as star-formation rate indicators because of the impact of extremely harsh environments on PAHs.

In the future, detailed studies such as this carried out across the whole NIR–MIR spectral range could be performed for samples of more distant and faint galaxies using the unprecedented spatial resolution (improvement of a factor of 10 with respect to Spitzer/IRS) and sensitivity that will be afforded by the James Webb Space Telescope. Such studies will enable the detailed study of PAH emission as a function of distance from the central AGN and investigate changes in the PAH population exposed to extremely harsh environments.

DATA AVAILABILITY

The data underlying this article will be shared on reasonable request to the corresponding author.

REFERENCES

Aitken D. K., Roche P. F., 1985, MNRAS, 213, 777
Allain T., Leach S., Sedlmayr E., 1996, A&A, 305, 616
Allamandola L. J., Tielens A. G. G. M., Barker J. R., 1989, ApJS, 71, 733
Alonso-Herrero A., Ward M. J., Kotilainen J. K., 1996, MNRAS, 278, 902
Alonso-Herrero A. et al., 2014, MNRAS, 443, 2766
Alonso-Herrero A. et al., 2020, A&A, 639, A43
Armus L. et al., 2009, PASP, 121, 559
Assef R. J. et al., 2013, ApJ, 772, 26
Bassani L. et al., 1999, ApJS, 121, 473
Baum S. A. et al., 2010, ApJ, 710, 289
Bauschlicher C. W., Peeters E., Allamandola L. J., 2008, ApJ, 678, 316
Binggeli B., Sandage A., Tammann G. A., 1985, AJ, 90, 1681
Brandl B. R. et al., 2006, ApJ, 653, 1129
Brightman M., Nandra K., 2011, MNRAS, 413, 1206
Cappi M. et al., 2006, A&A, 446, 459
de Grijp M. H. K., Lub J., Miley G. K., 1987, A&AS, 70, 95
Diamond-Stanic A. M., Rieke G. H., 2010, ApJ, 724, 140
Diamond-Stanic A. M., Rieke G. H., 2012, ApJ, 746, 168
Díaz-Santos T., Alonso-Herrero A., Colina L., Ryder S. D., Knapen J. H., 2007, ApJ, 661, 149
Dicken D. et al., 2012, ApJ, 745, 172
Dicken D. et al., 2014, ApJ, 788, 98
Draine B. T., Li A., 2001, ApJ, 551, 807
Draine B. T., Li A., 2007, ApJ, 657, 810
Draine B. T., Li A., Hensley B. S., Hunt L. K., Sandstrom K., Smith J.-D. T., 2020, ApJ, 917, 3
Esparza-Arredondo D. et al., 2018, ApJ, 859, 124
Esquej P. et al., 2014, ApJ, 780, 86
Fasano G., Franceschini A., 1987, MNRAS, 225, 155

Fazio G. G. et al., 2004, ApJS, 154, 10

Galliano F., Madden S. C., Tielens A. G. G. M., Peeters E., Jones A. P., 2008, ApJ, 679, 310

Gallimore J. F. et al., 2010, ApJS, 187, 172

García-Bernete I. et al., 2015, MNRAS, 449, 1309

García-Bernete I. et al., 2016, MNRAS, 463, 3531

García-Bernete I., Ramos Almeida C., Landt H., Ward M. J., Baloković M., Acosta-Pulido J. A., 2017, MNRAS, 469, 110

García-Bernete I. et al., 2019, MNRAS, 486, 4917

Gleisinger R. C., O'Dea C. P., Gallimore J. F., Wykes S., Baum S. A., 2020, ApJ, 905, 42

Gonzalez Delgado R. M., Perez E., 1997, MNRAS, 284, 931

González Delgado R. M., Heckman T., Leitherer C., 2001, ApJ, 546, 845

Groves B., Dopita M., Sutherland R., 2006, A&A, 458, 405

Guainazzi M., Matt G., Perola G. C., 2005, A&A, 444, 119

Helou G., Walker D. W., 1988, Infrared astronomical satellite (IRAS) catalogs and atlases, 7, 1

Hernán-Caballero A. et al., 2015, ApJ, 803, 109

Hernán-Caballero A. et al., 2020, MNRAS, 497, 4614

Ho L. C., Keto E., 2007, ApJ, 658, 314

Horst H., Gandhi P., Smette A., Duschl W. J., 2008, A&A, 479, 389

Houck J. R. et al., 2004, ApJS, 154, 18

Ichikawa K., Ueda Y., Terashima Y., Oyabu S., Gandhi P., Matsuta K., Nakagawa T., 2012, ApJ, 754, 45

Ichikawa K., Imanishi M., Ueda Y., Nakagawa T., Shirahata M., Kaneda H., Oyabu S., 2014, ApJ, 794, 139

Inami H. et al., 2018, A&A, 617, A130

Jensen J. J. et al., 2017, MNRAS, 470, 3071

Jourdain de Muizon M., D'Hendecourt L. B., Geballe T. R., 1990, A&A, 227, 526

Kennicutt R. C. et al., 2003, PASP, 115, 928

Kessler M. F. et al., 1996, A&A, 500, 493

Kewley L. J., Groves B., Kauffmann G., Heckman T., 2006, MNRAS, 372, 961

LaMassa S. M., Heckman T. M., Ptak A., Martins L., Wild V., Sonnentrucker P., 2010, ApJ, 720, 786

Lebouteiller V., Barry D. J., Spoon H. W. W., Bernard-Salas J., Sloan G. C., Houck J. R., Weedman D. W., 2011, ApJS, 196, 8

Li A., 2020, NatAs, 4, 339

Low F. J., Huchra J. P., Kleinmann S. G., Cutri R. M., 1988, ApJ, 327, L41

Lyu J., Rieke G. H., 2018, ApJ, 866, 92

Maiolino R., Rieke G. H., 1995, ApJ, 454, 95

Maiolino R., Ruiz M., Rieke G. H., Papadopoulos P., 1997, ApJ, 485, 552

Maragkoudakis A., Peeters E., Ricca A., 2020, MNRAS, 494, 642

Mateos S. et al., 2012, MNRAS, 426, 3271

McKinney J. et al., 2021, ApJ, 908, 238

Metropolis N., Rosenbluth A. W., Rosenbluth M. N., Teller A. H., Teller E., 1953, J. Chem. Phys., 21, 1087

Mori T. I., Sakon I., Onaka T., Kaneda H., Umehata H., Ohsawa R., 2012, ApJ, 744, 68

Mould J. R. et al., 2000, ApJ, 529, 786

Murakami H. et al., 2007, PASJ, 59, S369

Murga M. S., Kirsanova M. S., Vasyunin A. I., Pavlyuchenkov Y. N., 2020, MNRAS, 497, 2327

Nemmen R. S., Storchi-Bergmann T., Yuan F., Eracleous M., Terashima Y., Wilson A. S., 2006, ApJ, 643, 652

Onaka T. et al., 2007, PASJ, 59, S401

Ossenkopf V., Henning T., Mathis J. S., 1992, A&A, 261, 567

Peacock J. A., 1983, MNRAS, 202, 615

Peeters E., Hony S., Van Kerckhoven C., Tielens A. G. G. M., Allamandola L. J., Hudgins D. M., Bauschlicher C. W., 2002, A&A, 390, 1089

Peeters E., Spoon H. W. W., Tielens A. G. G. M., 2004, ApJ, 613, 986

Pereira-Santaella M. et al., 2010a, ApJS, 188, 447

Pereira-Santaella M., Diamond-Stanic A. M., Alonso-Herrero A., Rieke G. H., 2010b, ApJ, 725, 2270

Ramos Almeida C. et al., 2014, MNRAS, 445, 1130

Rayner J. T. et al., 2003, PASP, 115, 362

Reach W. T., Boulanger F., Contursi A., Lequeux J., 2000, A&A, 361, 895

Ricci C., Ueda Y., Koss M. J., Trakhtenbrot B., Bauer F. E., Gandhi P., 2015, ApJ, 815, L13

Ricci C. et al., 2017, ApJS, 233, 17

Riffel R., Rodríguez-Ardila A., Pastoriza M. G., 2006, A&A, 457, 61

Rigopoulou D., Spoon, H. W.W, Genzel R., Lutz D., Moorwood A. F. M., Tran Q. D., 1999, AJ, 118, 2625

Rigopoulou D., Kunze D., Lutz D., Genzel R., Moorwood A. F. M., 2002, A&A, 389, 374

Rigopoulou D. et al., 2021, MNRAS, 504, 5287

Risaliti G., Maiolino R., Salvati M., 1999, ApJ, 522, 157

Roche P. F., Aitken D. K., Smith C. H., Ward M. J., 1991, MNRAS, 248, 606

Rodríguez-Ardila A., Viegas S. M., 2003, MNRAS, 340, L33

Ruiterkamp R., Cox N. L. J., Spaans M., Kaper L., Foing B. H., Salama F., Ehrenfreund P., 2005, A&A, 432, 515

Sales D. A., Pastoriza M. G., Riffel R., 2010, ApJ, 725, 605

Sales D. A., Ruschel-Dutra D., Pastoriza M. G., Riffel R., Winge C., 2014, MNRAS, 441, 630

Sanders D. B., Mazzarella J. M., Kim D.-C., Surace J. A., Soifer B. T., 2003, AJ, 126, 1607

Shannon M. J., Boersma C., 2019, ApJ, 871, 124

Shu X. W., Wang J. X., Jiang P., Fan L. L., Wang T. G., 2007, ApJ, 657, 167

Siebenmorgen R. et al., 2004, A&A, 414, 123

Siebenmorgen R. et al., 2008, A&A, 488, 83

Smith J. D. T. et al., 2007a, ApJ, 656, 770

Smith J. D. T. et al., 2007b, PASP, 119, 1133

Sosa-Brito R. M., Tacconi-Garman L. E., Lehnert M. D., Gallimore J. F., 2001, ApJS, 136, 61

Spinoglio L., Andreani P., Malkan M. A., 2002, ApJ, 572, 105

Stanghellini L. et al., 2007, ApJ, 671, 1669

Stern D. et al., 2012, ApJ, 753, 30

ter Braak C. J. F., Vrugt J. A., 2008, Stat. Comput., 18, 435

Thornley M. D., Schreiber N. M. F., Lutz D., Genzel R., Spoon H. W. W., Kunze D., Sternberg A., 2000, ApJ, 539, 641

Tielens A. G. G. M., 2008, ARA&A, 46, 289

Tielens A. G. G. M., 2013, Planets, Stars and Stellar Systems, 5, 499

Tueller J., Mushotzky R. F., Barthelmy S., Cannizzo J. K., Gehrels N., Markwardt C. B., Skinner G. K., Winter L. M., 2008, ApJ, 681, 113

Ueda Y. et al., 2015, ApJ, 815, 1

Véron-Cetty M.-P., Véron P., 2006, A&A, 455, 773

Voit G. M., 1992, MNRAS, 258, 841

Weaver K. A. et al., 2010, ApJ, 716, 1151

Whittle M., 1992, ApJS, 79, 49

Wilson A. S., Helfer T. T., Haniff C. A., Ward M. J., 1991, ApJ, 381, 79

Winter L. M., Mushotzky R. F., Reynolds C. S., Tueller J., 2009, ApJ, 690, 1322

Winter L. M., Lewis K. T., Koss M., Veilleux S., Keeney B., Mushotzky R. F., 2010, ApJ, 710, 503

Wright E. L. et al., 2010, AJ, 140, 1868

Wu H. et al., 2005, ApJ, 632, L79

Wu Y., Helou G., Armus L., Cormier D., Shi Y., Dale D., Dasyra K. et al., 2010, ApJ, 723, 895

Yuan T.-T., Kewley L. J., Sanders D. B., 2010, ApJ, 709, 884

SUPPORTING INFORMATION

Supplementary data are available at MNRAS login.

online_appendices.pdf

Please note: Oxford University Press is not responsible for the content or functionality of any supporting materials supplied by the authors. Any queries (other than missing material) should be directed to the corresponding author for the article.

This paper has been typeset from a TeX/LaTeX file prepared by the author.